High-Pressure Synthesis, Crystal Structures, and Properties of A-Site Columnar-Ordered Quadruple Perovskites $NaRMn_2Ti_4O_{12}$ with R = Sm, Eu, Gd, Dy, Ho and Y

Ran Liu,[†,‡] Rebecca Scatena,[∀] Dmitry D. Khalyavin,[§] Roger D. Johnson,[##] Yoshiyuki Inaguma,[† †] Masahiko Tanaka,[§§] Yoshitaka Matsushita,[#] Kazunari Yamaura,[†,‡] and Alexei A. Belik[*,†]

[†] *International Center for Materials Nanoarchitectonics (WPI-MANA), National Institute for Materials Science (NIMS), Namiki 1-1, Tsukuba, Ibaraki 305-0044, Japan*

[‡] *Graduate School of Chemical Sciences and Engineering, Hokkaido University, North 10 West 8, Kita-ku, Sapporo, Hokkaido 060-0810, Japan*

[∀] *Clarendon Laboratory, Department of Physics, University of Oxford, Parks Road, Oxford, OX1 3PU, United Kingdom*

[§] *ISIS Facility, Rutherford Appleton Laboratory, Chilton, Didcot, OX11 0QX, United Kingdom*

[##] *Department of Physics and Astronomy, University College London, Gower Street, London, WC1E 6BT, United Kingdom*

[† †] *Department of Chemistry, Faculty of Science, Gakushuin University, 1-5-1 Mejiro, Toshima-ku, Tokyo 171-8588, Japan*

[§§] *Synchrotron X-ray Station at SPring-8, NIMS, Kouto 1-1-1, Sayo-cho, Hyogo 679-5148, Japan*

[#] *National Institute for Materials Science (NIMS), Sengen 1-2-1, Tsukuba, Ibaraki 305-0047, Japan*

Abstract

The formation of $NaRMn_2Ti_4O_{12}$ compounds (R = rare earth) under high pressure (about 6 GPa) and high temperature (about 1750 K) conditions was studied. Such compounds with R = Sm, Eu, Gd, Dy, Ho, and Y adopt the A-site columnar-ordered quadruple perovskite structure with a generic chemical formula $A_2A'A''B_4O_{12}$. Their crystal structures were studied by powder synchrotron X-ray and neutron diffraction between 1.5 and 300 K. They maintain a paraelectric structure, crystallizing in the centrosymmetric space group $P4_2/nmc$ (No. 137) at all temperatures, in comparison with the related $CaMnTi_2O_6$ perovskite in which a ferroelectric transition occurs at 630 K (*Chem. Mater*. **2014**, *26*, 2601-2608). The centrosymmetric structure was also confirmed by second-harmonic generation. They have a cation distribution of $[Na^+R^{3+}]_A[Mn^{2+}]_{A'}[Mn^{2+}]_{A''}[Ti^{4+}{}_4]_BO_{12}$ (to match with the generic chemical formula) with statistical distributions of Na^+ and R^{3+} at the large A site and a strongly split position of Mn^{2+} at the square-planar A′ site. We found a C-type long-range antiferromagnetic structure of Mn^{2+} ions at the A′ and A″ sites below T_N = 12 K for R = Dy, and found that the presence of Dy^{3+} disturbs the long-range ordering of Mn^{2+} below a second transition at lower temperatures. The first magnetic transition occurs below 8-13 K in all compounds, but the second magnetic transition occurs only for R = Dy, Sm and Eu. All compounds show large dielectric constant of a possible extrinsic origin similar to $CaCu_3Ti_4O_{12}$. $NaRMn_2Ti_4O_{12}$ with R = Er-Lu crystallized in the $GdFeO_3$-type *Pnma* perovskite structure, and $NaRMn_2Ti_4O_{12}$ with R = La and Nd contained two perovskite phases: an $AA'_3B_4O_{12}$-type *Im*-3 phase and a $GdFeO_3$-type *Pnma* phase.

1. Introduction

ABO_3 perovskite materials containing titanium at the octahedral B site ($B = Ti^{4+}$) have crucial and widespread applications in modern technologies that originate from exceptional dielectric, ferroelectric, and piezoelectric properties of such materials.[1-3] They constantly attract the attention of researchers working in the fields of fundamental and applied science.

$BaTiO_3$ and $PbTiO_3$ perovskites exhibit ferroelectric transitions at about 405 and 763 K, respectively. $BaTiO_3$ shows a further two phase transitions to other ferroelectric phases below 278 and 185 K.[2,4] Zr-doped $PbTiO_3$ perovskites are still the best piezoelectric materials for actuator and sensor applications in electronic devices.[2,3] $SrTiO_3$ is an archetypal incipient ferroelectric or a quantum paraelectric with changes of dielectric constant from about 370 at room temperature to about 18000 at 1.5 K.[5] This property attracted great attention to $SrTiO_3$; and ferroelectricity in $SrTiO_3$ could be triggered by isotope substitutions and strain engineering.[6,7] $SrTiO_3$ has wide applications, for example, as a substrate for thin film growths. $CaTiO_3$ crystallizes in the $GdFeO_3$-type *Pnma* structure at room temperature, and it shows no further symmetry changes on cooling and no ferroelectricity.[4] $CaTiO_3$ was also considered to be a quantum paraelectric. $CdTiO_3$, like $CaTiO_3$, crystallizes in the $GdFeO_3$-type *Pnma* structure at room temperature, but it undergoes a ferroelectric transition below about 85 K.[4,8]

Divalent cations at the A sites of $ATiO_3$ perovskites can be replaced for a 1:1 mixture of monovalent and trivalent cations. $Na_{0.5}R_{0.5}TiO_3$ compounds with R = rare-earth cations crystallize in the $GdFeO_3$-type *Pnma* structure, show no ferroelectric transitions, and were suggested to have quantum paraelectric behaviors.[9,10] On the other hand, $Na_{0.5}Bi_{0.5}TiO_3$ shows complex phase transformations, the appearance of ferroelectric phases, complex and hierarchical ferroelectric domains, and strong and anisotropic diffuse scattering.[11] $Na_{0.5}Bi_{0.5}TiO_3$ also forms morphotropic phase boundaries in different solid solutions and is considered as a promising lead-free piezoelectric material to replace toxic lead in Zr-doped $PbTiO_3$ perovskites.[12]

Giant dielectric constant, which was temperature independent in wide temperature ranges, was discovered in an A-site-ordered quadruple perovskite $CaCu_3Ti_4O_{12}$ containing Ti^{4+} at the B site.[13,14] The origin of such an exceptional property has been the subject of considerable investigation, and different mechanisms have been suggested in the literature.

Nowadays the most accepted picture involves the electrical inhomogeneity of $CaCu_3Ti_4O_{12}$ ceramics, with semiconducting grains and insulating grain boundaries that create an internal barrier layer capacitor effect.[15,16] The idea of replacing Ca^{2+} in $CaCu_3Ti_4O_{12}$ for a mixture of $0.5Na^+$ and $0.5R^{3+}$ was also applied in the literature, and the resulting $(Na_{0.5}R_{0.5})Cu_3Ti_4O_{12}$ materials showed interesting dielectric properties.[17,18]

Recently, a new mechanism for ferroelectricity was suggested in a $CaMnTi_2O_6$ perovskite containing Ti^{4+} at the B site.[19,20] This compound has a ferroelectric transition at 630 K, a long-range antiferromagnetic transition at 10 K, and switchable polarization at room temperature. It crystallizes in another subfamily of the perovskite structure – in the so-called A-site columnar-ordered quadruple perovskite structure with a generic chemical formula $A_2A'A''B_4O_{12}$.[21] Such perovskites have one column consisting of the AO_{10} polyhedra and one column consisting of alternating square-planar $A'O_4$ units and $A''O_4$ tetrahedra; the B sublattice is formed by corner-shared BO_6 octahedra as in all other (oxygen stoichiometric) perovskites. $CaMnTi_2O_6$ crystallizes in space group $P4_2/nmc$ (No. 137) above 630 K, and in space group $P4_2mc$ (No. 105) below 630 K.[19,20]

In this work, we investigated effects of the replacement of $2Ca^{2+}$ cations in $CaMnTi_2O_6$ for a mixture of Na^+ and R^{3+} cations, where R^{3+} is a rare-earth cation. We could prepare $NaRMn_2Ti_4O_{12}$ with R = Sm, Eu, Gd, Dy, Ho, and Y using a high-pressure, high-temperature method. We found that they maintain the paraelectric structure of $CaMnTi_2O_6$ between 1.5 and 300 K and crystallize in space group $P4_2/nmc$. Mn^{2+} cations remain highly disordered at the square-planar A′ site. They show large dielectric constant of a possible extrinsic origin similar to $CaCu_3Ti_4O_{12}$. Magnetic and specific heat measurements showed long-range magnetic ordering in all compounds below about 12 K, and C-type antiferromagnetic ordering of Mn^{2+} cations at the A′ and A″ sites was confirmed by neutron diffraction for R = Dy. However, certain magnetic rare-earth elements disturb the long-range ordering of Mn^{2+}, resulting in a second transition at lower temperatures.

2. Experimental Section

$NaRMn_2Ti_4O_{12}$ with R = La, Nd, Sm, Eu, Gd, Dy-Lu, and Y were prepared from stoichiometric mixtures of MnO, 'Na_2TiO_3', and commercial R_2O_3 (99.9-99.99 %) and

TiO_2 (99.99 %) at 6 GPa and about 1750 K for 2 h (heating time to the synthesis temperature was 10 min) in Pt capsules using a belt-type high-pressure apparatus. After heat treatments, the samples were quenched to room temperature (RT), and the pressure was slowly released. The temperature of our high-pressure apparatus is controlled by the heating power with a calibrated relationship between power and temperature. All samples were dark-brown hard pellets; powder (after grinding the pellets) was brownish orange. All R_2O_3 chemicals were dried at 1273 K for several hours before use. Single-phase MnO was prepared from commercial MnO_2 (99.99 %) by annealing at 1273 K in a 20 % H_2 + 80 % Ar flow for 2 h. 'Na_2TiO_3' was prepared by annealing of a stoichiometric mixture of TiO_2 and commercial Na_2CO_3 (99 %) at 1073 K for 100 h in air with several intermediate grindings. 'Na_2TiO_3' was a mixture of β-Na_2TiO_3 and $Na_8Ti_5O_{12}$ by X-ray diffraction.

X-ray powder diffraction (XRPD) data were collected at RT on a RIGAKU MiniFlex600 diffractometer using CuKα radiation (2θ range of 8–100 °, a step width of 0.02 °, and scan speed of 1 °/min). High-temperature XRPD data of $NaSmMn_2Ti_4O_{12}$ were measured on a RIGAKU SmartLab instrument using CuKα_1 radiation (45 kV, 200 mA; 2θ range of 5–100 °, a step width of 0.02°, and scan speed of 1 °/min) from 300 K to 770 K and from 770 K to 300 K using a furnace attachment. Synchrotron XRPD data were measured at RT on a large Debye-Scherrer camera at the undulator beamline BL15XU of SPring-8.[22,23] The intensity data were collected between 2 ° and 60.23 ° at 0.003 ° intervals in 2θ; the incident beam was monochromatized at λ = 0.65298 Å. The samples were packed into Lindemann glass capillaries (inner diameter: 0.1 mm), which were rotated during measurements. Absorption coefficients were also measured. The Rietveld analysis was performed using the *RIETAN-2000* program.[24] Weight fractions of phases (mass %) reported in this work were estimated by *RIETAN-2000* from the refined scale factors after the Rietveld analysis of synchrotron XRPD data.

Neutron powder diffraction data of $NaDyMn_2Ti_4O_{12}$ were collected at the ISIS pulsed neutron and muon spallation source at the Rutherford Appleton Laboratory (UK), using the WISH diffractometer located at the second target station.[25] The sample (~1.88 g: samples from 4 capsules were mixed) was loaded into a cylindrical 3 mm diameter vanadium can and measured at 1.5-20 K. Rietveld refinements of the crystal and magnetic structures were

performed using the *FullProf* program[26] against the data measured in detector banks at average 2θ values of 58°, 90°, 122°, and 154°, each covering 32° of the diffraction plane.

Powder second-harmonic-generation (SHG) measurements for $NaRMn_2Ti_4O_{12}$ with R = Sm and Gd were performed at room temperature on a modified Kurtz[27] nonlinear optical system using 1064 nm light in order to check the presence or absence of centrosymmetry. The experimental details are described in Ref. 28.

Magnetic measurements were performed on a SQUID magnetometer (Quantum Design, MPMS-XL-7T) between 2 and 400 K in different applied fields under both zero-field-cooled (ZFC) and field-cooled on cooling (FCC) conditions. The inverse magnetic susceptibilities (χ^{-1}) were fit by the Curie-Weiss equation

$$\chi(T) = \mu_{\text{eff}}^2 N(3k_B(T-\theta))^{-1} \qquad (1)$$

where μ_{eff} is the effective magnetic moment, N is Avogadro's number, k_B is Boltzmann's constant, and θ is the Curie-Weiss temperature. For fitting, we used the FCC curves measured at 10 kOe and temperature intervals between 200 and 395 K. Isothermal magnetization measurements were performed between –70 and 70 kOe (at T = 1.8 and 5 K) and between –10 and 10 kOe (at T = 2 K). Frequency dependent ac susceptibility measurements were performed on cooling with a Quantum Design MPMS-1T instrument at different frequencies (f) and different applied oscillating magnetic fields (H_{ac}). Specific heat, C_p, at magnetic fields of 0 and 90 kOe was recorded between 2 and 100 K on cooling by a pulse relaxation method using a commercial calorimeter (Quantum Design PPMS). Dielectric properties were measured on a Quantum Design PPMS using a NOVOCONTROL Alpha-A High Performance Frequency Analyzer between 3 and 330 K on cooling and heating in the frequency range of 100 Hz and 2 MHz and at zero magnetic field in usual vacuum and high vacuum conditions of the PPMS. Under usual vacuum conditions, contributions from ice (most probably) to the dielectric constant were observed between about 220 and 270 K (depending on frequency). The extrinsic (ice) contribution disappeared under high vacuum conditions; however, below about 50 K, the real sample temperature deviated significantly from the system temperature. Therefore, dielectric measurements under usual vacuum and high vacuum conditions were combined to obtain dielectric data in the whole temperature range.

Differential scanning calorimetry (DSC) curves were recorded on a Mettler Toledo DSC1 STAR^e system at a heating/cooling rate of 10 K/min under an N_2 flow between 290 K and 723-873 K in open Al capsules and between 290 K and 973 K in open Pt capsules. Several DSC runs were performed to check the reproducibility.

3. Results and Discussion

3.1. Phase Compositions. $NaRMn_2Ti_4O_{12}$ with R = Nd contained two perovskites phases: an A-site-ordered quadruple perovskite phase $(Nd_{0.8}Na_{0.2})Mn_3(Ti_{0.925}Mn_{0.075})_4O_{12}$ with space group *Im*-3 (about 75 mass %; *a* = 7.55000(2) Å) and a $GdFeO_3$-type *Pnma* perovskite phase $(Nd_{0.5}Na_{0.5})TiO_3$ (about 23 mass %; *a* = 5.43738(5) Å, *b* = 7.68966(6) Å, and *c* = 5.42755(5) Å) plus TiO_2 impurity (about 2 mass %). Note that the compositions of the A sites in both perovskite-related phases for R = Nd and the given lattice parameters were obtained by analysis of synchrotron XRPD data (Table S1 and Figure S1). A similar phase composition was found in the case of R = La. $NaRMn_2Ti_4O_{12}$ with R = Er-Lu contained a $GdFeO_3$-type *Pnma* perovskite phase, whose formula can be presented as $(Na_{0.25}R_{0.25}Mn_{0.5})TiO_3$, and a TiO_2 impurity (about 2-3 mass %). For example, the lattice parameters refined from synchrotron XRPD data at RT were *a* = 5.39602(2) Å, *b* = 7.54442(2) Å, and *c* = 5.23484(2) Å for R = Er and *a* = 5.39584(2) Å, *b* = 7.53471(2) Å, and *c* = 5.22424(2) Å for R = Yb.

$NaRMn_2Ti_4O_{12}$ with R = Sm, Eu, Gd, Dy, Ho, and Y mainly consisted of a new perovskite phase, whose reflections could be indexed in a tetragonal system. The subsequent structural analysis showed that they adopt the parent structure of the A-site columnar-ordered quadruple perovskite family with space group $P4_2/nmc$ (No. 137).[21,29] They all contained about 2-4 mass % of TiO_2 impurity; $NaRMn_2Ti_4O_{12}$ with R = Ho and Y also contained about 8 mass % of a $GdFeO_3$-type *Pnma* perovskite phase. The SHG response was not detected for $NaRMn_2Ti_4O_{12}$ with R = Sm and Gd at RT. Therefore, SHG measurements confirmed a centrosymmetric space group.

The above results show that for $NaRMn_2Ti_4O_{12}$, the A-site columnar-ordered quadruple perovskite structure is stabilized for the middle-size rare-earth elements of R = Sm-Ho and Y, with a transition region at R = Ho and Y to the $GdFeO_3$-type *Pnma* perovskite structure.

$NaTbMn_2Ti_4O_{12}$ should also crystallize in the same structure as the samples with R = Sm-Ho and Y, but we did not prepare it because a high-quality Tb_2O_3 chemical is not readily available. These results provide further evidence that the stability of A-site columnar-ordered quadruple perovskites in general strongly depends on the occupation of the A′, A″, and B sites, and that it is considerably limited.[21] For example, $R_2MnMn(Mn_2Sb_2)O_{12}$ is stable for R = La-Sm (at synthesis conditions used for all examples),[30] $R_2MnMnMn_4O_{12}$ is stable for R = Gd-Er and Y,[31] $R_2CuMnMn_4O_{12}$ is stable for R = Dy-Lu and Y,[32] and $R_2MnMn(MnTi_3)O_{12}$ is stable for R = Nd-Gd.[33]

Figure 1 gives the compositional dependence of the lattice parameters in $NaRMn_2Ti_4O_{12}$. The lattice parameters change monotonically as a function of the ionic radii of the R^{3+} cations in a 10-fold coordination.[34] As the ionic radii in a 10-fold coordination are not available for the majority of R^{3+} cations we used the ionic radii in an 8-fold coordination plus 0.105 Å (the average difference between the ionic radii in 8- and 9-fold coordination is 0.055 Å, and the average difference between the ionic radii in 9- and 10-fold coordination is 0.05 Å).[34]

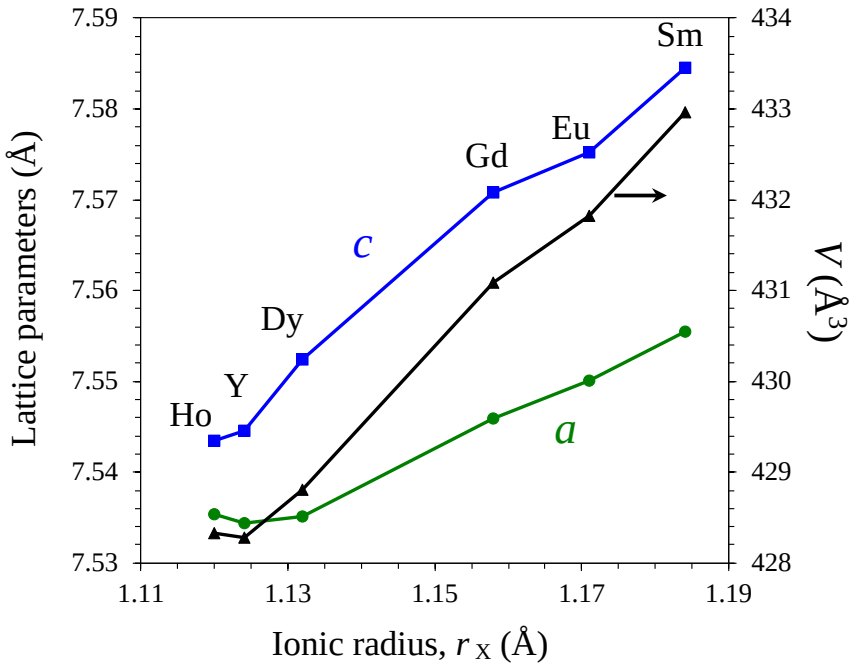

Figure 1. Compositional dependence of the room-temperature lattice parameters (*a* and *c*; space group $P4_2/nmc$) in $NaRMn_2Ti_4O_{12}$ as a function of the ionic radius of R^{3+} cations in the 10-fold coordination (see the text for details).

3.2. Crystal Structures. In the following analysis of the $NaRMn_2Ti_4O_{12}$ (R = Sm, Eu, Gd, Dy, Ho, and Y) crystal structures we selected $NaDyMn_2Ti_4O_{12}$ as a representative to facilitate comparison with neutron diffraction studies (see part 3.5). The initial structural model was taken from Ref. 33 for $Sm_2MnMn(Mn_{4-x}Ti_x)O_{12}$. It was confirmed that the A sites (in $A_2A'A''B_4O_{12}$) are statistically occupied by Na^+ and R^{3+} cations: the refined occupation factors were *g*(Dy) = 0.5033(9) and *g*(Na) = 0.4967. Therefore, the ideal 1:1 ratio of Na:R was fixed in the final refinements. The thermal parameter (*B*) of the square-planar Mn1 site (A′) in the ideal 2*a* (0.75, 0.25, 0.75) position was large for all the samples (*B*(Mn1) = 2.75(5) $Å^2$ for R = Dy), which indicated that the Mn1 site should be split. Indeed, moving Mn1 from the ideal 2*a* (0.75, 0.25, 0.75) position with *g*(Mn1) = 1 (where *g* is the occupation factor) to the 4*c* (0.75, 0.25, *z*) position with *g*(Mn1) = 0.5 significantly reduced the *B* parameter for the Mn1 site and *R* values (from R_{wp} = 3.14 %, R_P = 2.10 %, R_I = 4.57 %, R_F = 4.71 % for the ideal Mn1 site to R_{wp} = 2.52 %, R_P = 1.84 %, R_I = 4.11 %, R_F = 4.07 % for the split Mn1 site). No evidence for further anti-site cation disorder could be found from the synchrotron X-ray diffraction data analysis (Tables S2 and S3), where deviations of the occupation factors from the ideal values were small and correlated with the thermal parameters. To the contrary, neutron diffraction measurements (Section 3.5) indicated about 6 % Dy/Mn occupational disorder between A and (A′, A″) sites. We note that different synthetic batches of $NaDyMn_2Ti_4O_{12}$ were used for synchrotron and neutron diffraction experiments, and slightly different synthesis conditions (even though we used the same nominal synthesis conditions) could result in different cation distributions; the preparation of the neutron sample in a large volume could also affect the cation distribution.

Tables 1 and 2 give the refined structural parameters for all the samples. Table 3 summarizes the main bond lengths, bond-valence sum (BVS)[35] values, and Ti-O-Ti bond angles. Experimental, calculated, and difference synchrotron XRPD diffraction patterns of $NaDyMn_2Ti_4O_{12}$ are plotted in Figure 2a. Figure 3 illustrates the crystal structure of $NaDyMn_2Ti_4O_{12}$. Tables S4 and S5 compare synchrotron X-ray diffraction refinement

results for $NaDyMn_2Ti_4O_{12}$ with the ideal cation distribution (R_{wp} = 2.52 % and R_P = 1.84 %) and with the anti-site disorder established by neutron diffraction (R_{wp} = 3.01 % and R_P = 2.03 %).

Table 1. Structure Parameters of $NaRMn_2Ti_4O_{12}$ with R = Sm, Eu, and Gd

R	Sm	Eu	Gd
Source		Synchrotron X-ray	
Wavelength (Å)		0.65298	
d-space range (Å)		0.6506-6.238	
Crystal system		Tetragonal	
Space group		$P4_2/nmc$ (No. 137, cell choice 2)	
Z		2	
Temperature (K)		295	
Formula Weight (g/mol)	666.725	668.329	673.615
a (Å)	7.55548(1)	7.55009(1)	7.54595(2)
c (Å)	7.58456(2)	7.57526(2)	7.57080(5)
V (Å^3)	432.9665(17)	431.8192(14)	431.092(3)
z(Na/R)	0.22628(7)	0.22516(6)	0.22460(9)
B(Na/R) (Å^2)	0.360(10)	0.402(9)	0.400(14)
z($Mn1_{SQ}$)	0.7911(3)	0.7896(3)	0.7885(5)
B($Mn1_{SQ}$) (Å^2)	0.92(6)	0.80(5)	0.85(8)
B($Mn2_T$) (Å^2)	0.53(5)	0.53(4)	0.34(7)
B(Ti_O) (Å^2)	0.673(12)	0.657(10)	0.670(15)
y(O1)	0.0520(4)	0.0522(3)	0.0526(5)
z(O1)	–0.0376(4)	–0.0354(3)	–0.0356(5)
B(O1) (Å^2)	0.12(6)	0.03(5)	0.33(8)
y(O2)	0.5397(4)	0.5406(3)	0.5443(5)
z(O2)	0.5627(4)	0.5622(3)	0.5614(5)
B(O2) (Å^2)	0.31(6)	0.44(6)	0.35(8)
x(O3)	0.4523(3)	0.4514(2)	0.4524(4)
B(O3) (Å^2)	0.68(6)	0.83(6)	0.75(9)
R_{wp} (%)	2.82	2.19	2.39
R_p (%)	1.95	1.58	1.60
R_I (%)	4.19	5.94	4.22
R_F (%)	2.66	4.57	2.88
R_{exp} (%)	0.96	0.93	0.81

TiO_2 impurity (mass %)	3.6	2.0	1.9

Na/R – 4*d* site (0.25, 0.25, *z*); Mn1 – 4*c* site (0.75, 0.25, *z*) near 2*a* site (0.75, 0.25, 0.75); Mn2 – 2*b* site (0.75, 0.25, 0.25); Ti – 8*e* site (0, 0, 0); O1 and O2 – 8*g* site (0.25, *y*, *z*), and O3 – 8*f* site (*x*, –*x*, 0.25).
g(Mn2) = *g*(Ti) = *g*(O1) = *g*(O2) = *g*(O3) = 1, were *g* is the occupation factor, and *g*(Mn1) = 0.5 and *g*(Na/R) = 0.5Na + 0.5R.
SQ: square-planar, T: tetrahedral; O: octahedral.

Table 2. Structure Parameters of $NaRMn_2Ti_4O_{12}$ with R = Dy, Y, and Ho at T = 295 K from Synchrotron X-ray Powder Diffraction Data

R	Dy	Y	Ho
Formula Weight (g/mol)	678.865	605.233	681.257
a (Å)	7.53507(1)	7.53441(1)	7.53532(1)
c (Å)	7.55243(1)	7.54452(2)	7.54347(3)
V (Å^3)	428.8069(6)	428.2822(13)	428.3259(19)
z(Na/R)	0.22248(4)	0.22498(17)	0.22254(8)
B(Na/R) (Å^2)	0.464(6)	0.61(3)	0.616(12)
z(Mn1$_{SQ}$)	0.79279(17)	0.7916(4)	0.7903(4)
B(Mn1$_{SQ}$) (Å^2)	0.29(3)	0.49(7)	0.85(8)
B(Mn2$_T$) (Å^2)	0.45(3)	0.87(6)	0.65(7)
B(Ti$_O$) (Å^2)	0.595(8)	0.554(15)	0.460(15)
y(O1)	0.0539(3)	0.0593(6)	0.0528(5)
z(O1)	–0.0356(3)	–0.0370(5)	–0.0353(5)
B(O1) (Å^2)	0.31(4)	0.20(9)	0.31(8)
y(O2)	0.5436(2)	0.5408(5)	0.5474(5)
z(O2)	0.5619(2)	0.5596(5)	0.5596(5)
B(O2) (Å^2)	0.35(4)	0.55(8)	0.46(8)
x(O3)	0.45154(19)	0.4550(3)	0.4566(4)
B(O3) (Å^2)	0.78(4)	0.69(8)	1.22(10)
R_{wp} (%)	2.52	1.47	2.76
R_p (%)	1.84	1.08	1.87
R_I (%)	4.11	6.29	5.58
R_F (%)	4.04	6.97	4.21
R_{exp} (%)	1.11	0.70	0.97
TiO_2 impurity (mass %)	2.7	3.3	2.0
Pnma impurity (mass %)	-	8.3	8.3

Additional information is the same as in Table 1.

Table 3. Bond Lengths (in Å), Bond Angles (in °), Bond-Valence Sum (BVS), and Distortion Parameters of TiO_6 (Δ) in $NaRMn_2Ti_4O_{12}$ with R = Sm, Eu, Gd, Dy, Y, and Ho at *T* = 295 K

R	Sm	Eu	Gd	Dy	Y	Ho
Na/R-O1 (Å) ×2	2.334(3)	2.350(3)	2.348(4)	2.350(2)	2.300(4)	2.355(4)
Na/R-O1 (Å) ×2	2.498(3)	2.475(2)	2.470(4)	2.446(2)	2.443(3)	2.448(4)
Na/R-O2 (Å) ×2	2.516(3)	2.518(2)	2.541(3)	2.523(2)	2.521(4)	2.556(4)
Na/R-O3 (Å) ×4	2.725(1)	2.726(1)	2.723(1)	2.722(1)	2.713(1)	2.712(1)
BVS(R^{3+})	+3.03	+2.93	+2.83	+2.68	+2.66	+2.55
BVS(Na^{+})	+1.39	+1.39	+1.38	+1.42	+1.49	+1.39
0.5[BVS(R^{3+})+ BVS(Na^{+})]	+2.21	+2.16	+2.11	+2.05	+2.08	+1.97
BVS(Na/R)	+2.06	+2.02	+1.98	+1.95	+1.99	+1.88
Mn1-O3 (Å) ×4	2.184(3)	2.171(3)	2.179(4)	2.172(2)	2.206(4)	2.223(5)
Mn1-O2 (Å) ×2	2.602(3)	2.601(3)	2.585(5)	2.559(2)	2.567(5)	2.541(5)
Mn1-O1 (Å) ×2	2.950(3)	2.945(3)	2.952(4)	2.934(2)	2.979(5)	2.936(4)
Mn1-Mn1	0.624(4)	0.601(4)	0.582(7)	0.646(3)	0.620(5)	0.609(6)
BVS($Mn1^{2+}$)	+1.69	+1.74	+1.72	+1.77	+1.62	+1.59
BVS($Mn1i^{2+}$)	+1.69	+1.74	+1.72	+1.77	+1.63	+1.58
Mn2-O2 (Å) ×4	2.132(3)	2.126(3)	2.109(4)	2.107(2)	2.133(4)	2.096(4)
Mn2-O1 (Å) ×4	2.793(3)	2.802(2)	2.802(4)	2.805(2)	2.831(4)	2.798(4)
BVS($Mn2^{2+}$)	+1.85	+1.87	+1.95	+1.96	+1.83	+2.01
Ti-O1 (Å) ×2	1.950(1)	1.947(1)	1.947(1)	1.946(1)	1.956(1)	1.944(1)
Ti-O2 (Å) ×2	1.971(1)	1.970(1)	1.971(1)	1.969(1)	1.961(1)	1.969(1)
Ti-O3 (Å) ×2	1.963(1)	1.964(1)	1.960(1)	1.958(1)	1.946(1)	1.942(1)
Δ(Ti)	1.9×10^{-5}	2.4×10^{-5}	2.7×10^{-5}	2.2×10^{-5}	1.0×10^{-5}	4.2×10^{-5}
BVS(Ti^{4+})	+4.04	+4.06	+4.06	+4.09	+4.12	+4.15
Ti-O1-Ti ×2	151.17(8)	151.65(7)	151.46(8)	151.00(7)	148.75(8)	151.48(8)
Ti-O2-Ti ×2	146.86(8)	146.81(7)	146.25(8)	146.26(7)	147.74(8)	146.11(8)
Ti-O3-Ti ×2	149.92(8)	149.35(7)	149.95(8)	149.41(7)	151.48(8)	152.47(8)

BVS = $\sum_{i=1}^{N} v_i$, $v_i = \exp[(R_0 - l_i)/B]$, l_i is a bond length, N is the coordination number, B = 0.37, $R_0(Sm^{3+})$ = 2.088 Å, $R_0(Eu^{3+})$ = 2.076 Å, $R_0(Gd^{3+})$ = 2.065 Å, $R_0(Dy^{3+})$ = 2.036 Å, $R_0(Y^{3+})$ = 2.014 Å, $R_0(Ho^{3+})$ = 2.023 Å, $R_0(Na^{+})$ = 1.80 Å, $R_0(Mn^{2+})$ = 1.79 Å, $R_0(Ti^{4+})$ = 1.815 Å, R_0(Na/R) is the average value of $R_0(Na^{+})$ and $R_0(R^{3+})$.[35]

$\Delta = (1/N)\sum_{i=1}^{N}[(l_i - l_{av})/l_{av}]^2$, where $l_{av} = (1/N)\sum_{i=1}^{N} l_i$ is the average distance.

Mn1i is the ideal 2*a* site (0.75, 0.25, 0.75).

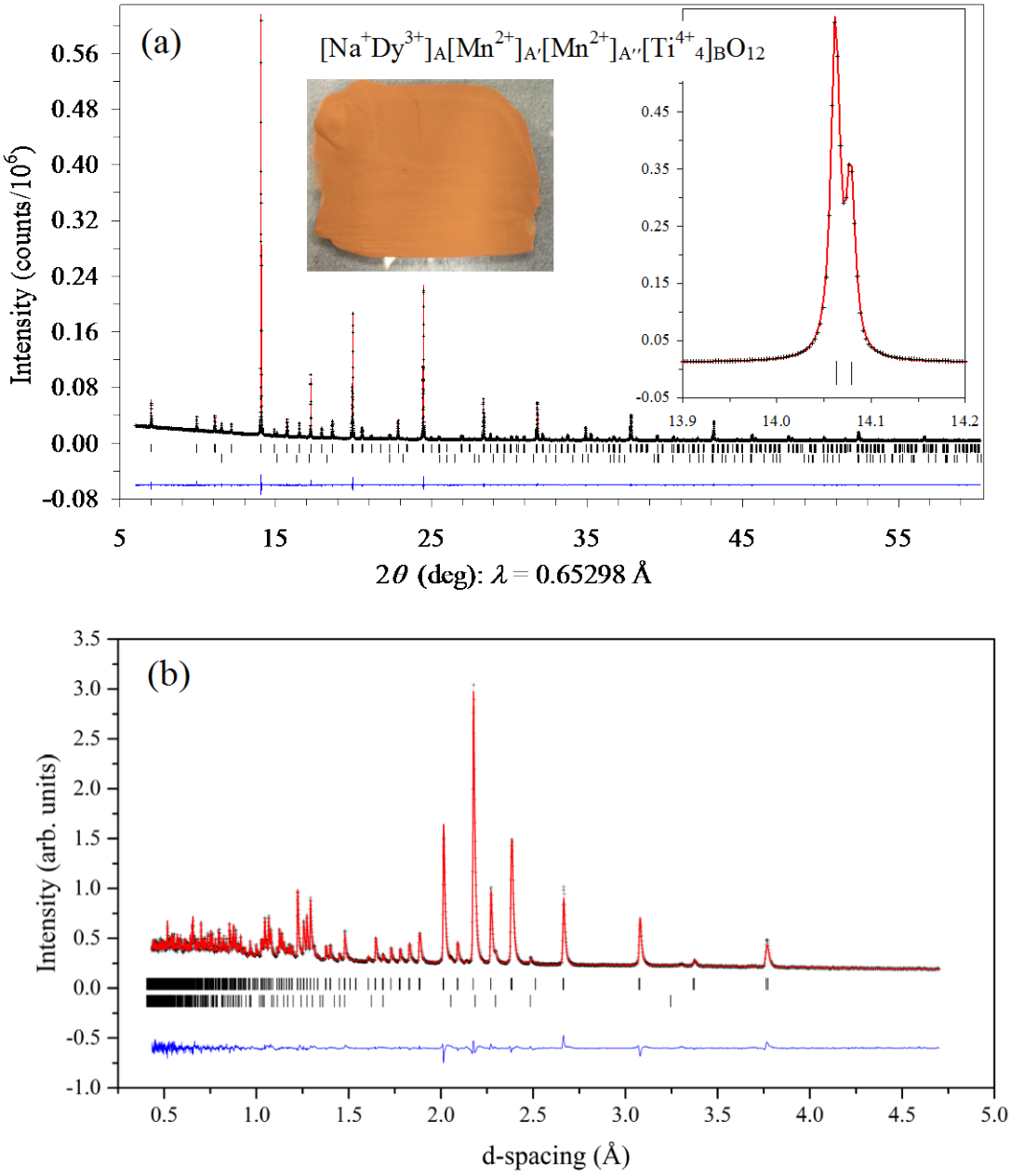

Figure 2. (a) Experimental (black crosses), calculated (red line), and difference (blue line) synchrotron X-ray powder diffraction patterns at T = 295 K and (b) neutron powder diffraction patterns at T = 20 K for $NaDyMn_2Ti_4O_{12}$. The tick marks show possible Bragg reflection positions for the main perovskite phase (the first row) and TiO_2 impurity (the

second row). The right inset in panel (a) shows an enlarged fragment near the strongest reflections. The left inset in panel (a) shows color of a powder $NaDyMn_2Ti_4O_{12}$ sample.

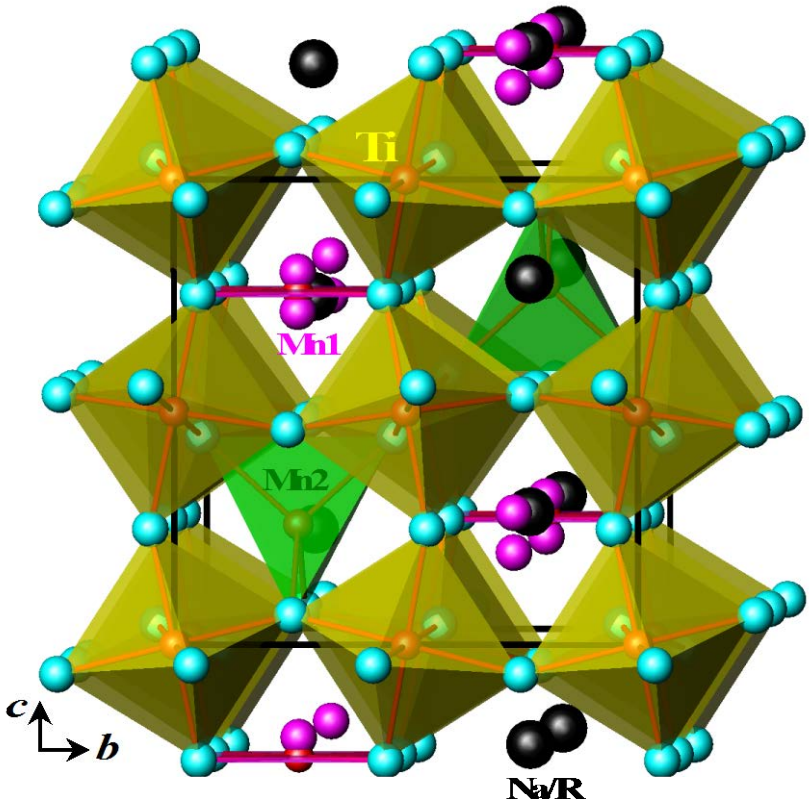

Figure 3. Crystal structure of $NaDyMn_2Ti_4O_{12}$. Ideal $Mn1O_4$ square-planar units, $Mn2O_4$ tetrahedra, and TiO_6 octahedra are shown. (Na/R) atoms are presented by large black spheres. The split Mn1 sites are also shown by pink spheres.

The BVS values for the Na/R site (+1.88 to +2.06), calculated using the average R_0 values (= $0.5[R_0(Na^+) + R_0(R^{3+})]$, that is, assuming the presence of a virtual $0.5Na^+/0.5R^{3+}$ atom), were close to the expected value of +2 for all samples. We also calculated separate BVS values for R^{3+} and Na^+ cations. The BVS(Na^+) values were about +1.4 for samples with R = Sm, Eu, Gd, Dy, and Ho, and +1.5 for R = Y, suggesting that Na^+ cations are always overbonded. The common BVS(Na^+) values originate from similar Na/R-O bond lengths (approx. 2.55 Å) found in all samples. Such rigidity in the bonding of the Na/R

cations originates from the structural features of the A-site columnar-ordered quadruple perovskites, where the octahedral tilts are primarily realized to establish a square-planar coordination for the Mn1 site and a tetrahedral coordination for the Mn2 site. On the other hand, the BVS values for R^{3+} cations reduce from +3.03 (R = Sm) to +2.55 (R = Ho) suggesting that smaller rare-earth cations are underbonded. Such underbonding of R^{3+} and overbonding of Na^{+} could determine the rare-earth stability range of these A-site columnar-ordered quadruple perovskites.

The Mn2-O2 bond lengths for the tetrahedral Mn2 site were within 2.096-2.133 Å in all samples as expected for Mn^{2+} cations, resulting in BVS values close to +2 (+1.83 to +2.01). The BVS values for the Ti site (+4.04 to +4.15) were close to the expected value of +4 for all samples, and the octahedral distortion parameter, $\Delta(TiO_6) = 1\text{-}4\times10^{-5}$ (the definition is given in note of Table 3), was very small suggesting a nearly regular TiO_6 octahedron in all the samples. Only the BVS values for the square-planar Mn1 site (+1.59 to +1.77) deviated noticeably from the expected value of +2. It is interesting that the BVS values were almost identical for the split Mn1 position and for the ideal Mn1 position; this fact could suggest that Mn^{2+} cations can move in a certain region. The distance between the split and ideal positions was about 0.3 Å in all the samples; the similar shifts of Mn^{2+} cations from the center of the square-planar units (0.3-0.4 Å) were observed in the ferroelectric and paraelectric phases of $CaMnTi_2O_6$.[19,20] The ideal cation distribution in $NaRMn_2Ti_4O_{12}$ can be presented as $[Na^{+}R^{3+}]_A[Mn^{2+}]_{A'}[Mn^{2+}]_{A''}[Ti^{4+}{}_4]_BO_{12}$ to match with a generic chemical formula $A_2A'A''B_4O_{12}$ for such perovskites.[21]

So far, A-site columnar-ordered quadruple perovskites were only reported with Ca^{2+} and R^{3+} cations at the A site. Our results showed that such perovskites can also accommodate Na^{+} cations at the A site.

3.3. Thermal Properties of $NaRMn_2Ti_4O_{12}$. High-temperature studies were performed prior to the detailed structural investigations described above in order to rule out, or confirm, the existence of a ferroelectric transition as observed in $CaMnTi_2O_6$.[19,20] The first heating DSC curves of $NaRMn_2Ti_4O_{12}$ exhibited broad peaks near 630-660 K (Figures S2 and S3). These temperatures are close to the ferroelectric transition temperature of 630 K in $CaMnTi_2O_6$[19,20] and could suggest the presence of such a transition in $NaRMn_2Ti_4O_{12}$. However, no anomalies were detected in all cooling DSC curves and on the second (and

third) heating DSC curves, suggesting that the DSC anomaly on the first heating curve is irreversible and is not caused by any structural phase transitions. Figure 4 shows the temperature dependence of the lattice parameters and unit cell volume of $NaSmMn_2Ti_4O_{12}$ during heating and cooling. The volumetric coefficient of thermal expansion of $NaSmMn_2Ti_4O_{12}$ has a typical value of the order of 10^{-5} K^{-1} between 300 and 750 K (Figure 4b).

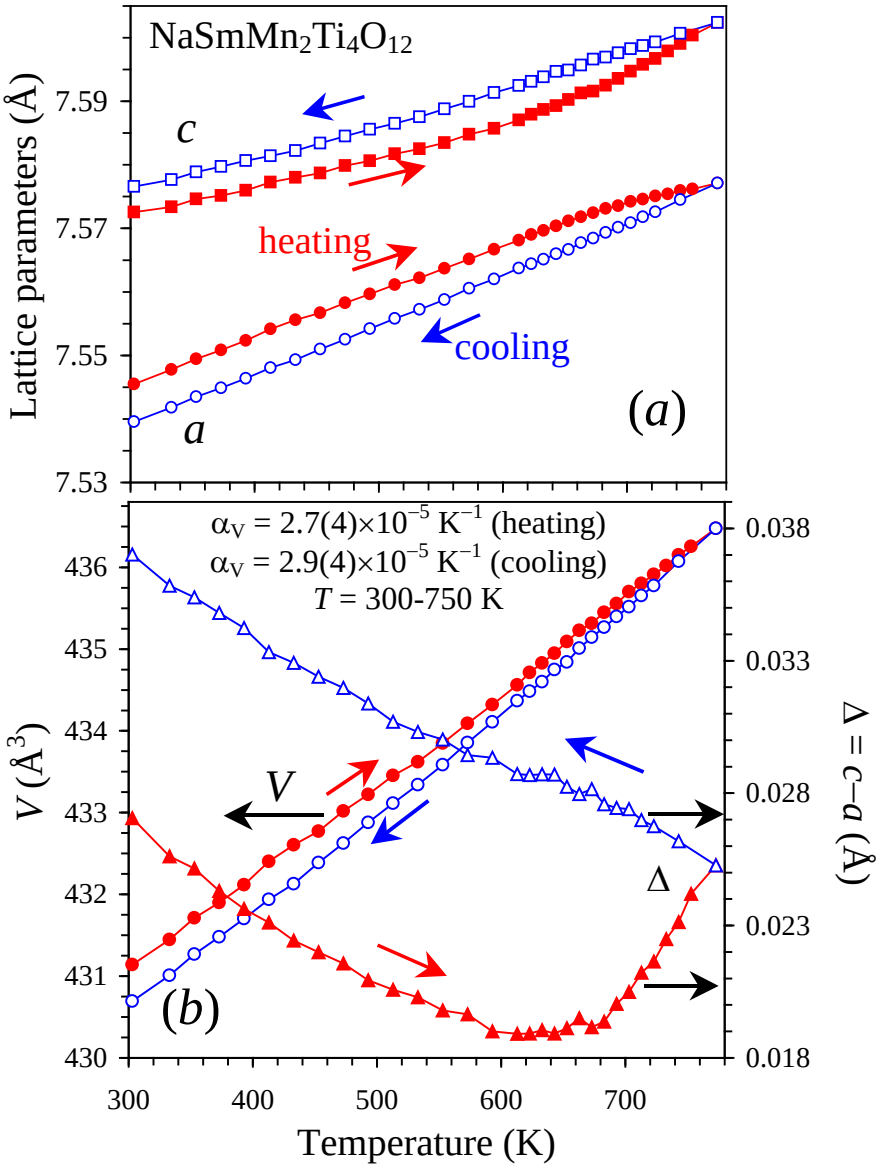

Figure 4. Temperature dependence of (a) the *a* and *c* lattice parameters and (b) unit-cell volume (the left-hand axis) and the difference between the *c* and *a* parameters (the

right-hand axis) in $NaSmMn_2Ti_4O_{12}$ during heating and cooling. α_V is the volumetric coefficient of thermal expansion.

On heating, the difference between the *a* and *c* parameters first decreases with increasing temperature up to about 600 K, but then it increases sharply above 650 K up to 770 K, where the DSC anomalies were observed. On cooling, the difference between the *a* and *c* parameters became monotonic again. In the case of $CaMnTi_2O_6$,[19,20] the difference between the *a* and *c* parameters rapidly decreases on heating in the ferroelectric $P4_2mc$ phase, and the *a* and *c* parameters almost merged in the paraelectric $P4_2/nmc$ phase above 630 K. The high-temperature behaviour of $NaRMn_2Ti_4O_{12}$ can probably be explained by annealing and relaxation effects of the metastable, stressed high-pressure phases, which were obtained by quenching. High-pressure and high-temperature synthesis conditions naturally introduce huge residual stresses in the as-prepared samples. Since the lattice is non-cubic, the elastic moduli can be different for the in-plane and out-of-plane directions, making the stresses anisotropic. Hence, the annealing procedure that releases the stresses will result in an anisotropic change of the lattice parameters. We note, however, that we cannot exclude small variations of the oxygen content during annealing. Irreversible behavior of the first DSC curves is often observed in high-pressure-synthesized samples,[36] and we also observed similar irreversible DSC anomalies at 630 and 645 K on the first heating curve of $NaYbMn_2Ti_4O_{12}$ (Figure S3). This sample crystallizes in a different *Pnma* perovskite structure, confirming that the high temperature DSC anomalies observed for the A-site columnar ordered quadruple perovskites are not caused by an intrinsic structural phase transition. After DSC experiments, all samples were checked by laboratory XRPD (at RT), and no noticeable changes in the phase compositions were found (that is, no new impurities appeared and the amount of TiO_2 impurity did not visibly change). After the DSC experiments and high-temperature XRPD experiment (Figure 4), the *a* lattice parameter showed a tendency to decrease (in comparison with the as-synthesized samples), while the *c* lattice parameter – a tendency to increase for all samples (Tables S6). $NaGdMn_2Ti_4O_{12}$ was heated up to 973 K, and $NaEuMn_2Ti_4O_{12}$ – up to 873 K; the samples remained stable at least up to these temperatures. We note that, as the $NaRMn_2Ti_4O_{12}$ compounds already adopt the parent A-site columnar-ordered quadruple perovskite crystal structure at room

temperature, higher temperature structural transitions are unlikely since any further symmetry increase will necessarily destroy the coordination environments for the Mn1 and Mn2 sites and hence likely lead to sample decomposition.

3.4. Magnetic Properties of $NaRMn_2Ti_4O_{12}$. Figures 5-7 show magnetic susceptibility curves (χ versus T) of $NaRMn_2Ti_4O_{12}$. The samples containing R^{3+} cations with large moments (R = Gd, Dy, and Ho) show no clear features on the χ versus T curves, which were dominated by paramagnetic-like contributions from R^{3+} cations. Weak anomalies at T_N could only be seen on the $d(\chi T)/dT$ versus T curves (insets of Figures 5-7). The samples containing R^{3+} cations with small moments (R = Sm and Eu) and non-magnetic R^{3+} cations (R = Y) showed small maxima at T_N. $NaSmMn_2Ti_4O_{12}$ exhibits two anomalies near T_{N1} = 10.5 K and T_{N2} = 5.0 K on the χ versus T curves at 100 Oe and 10 kOe. Two anomalies could also be seen on the 100 Oe $d(\chi T)/dT$ versus T curves of $NaEuMn_2Ti_4O_{12}$ near T_{N1} = 11.5 K and T_{N2} = 5.0 K. Figures S4-S11 provide results of ac susceptibility measurements for all $NaRMn_2Ti_4O_{12}$, where no ac field dependence was observed, and small frequency dependence was detected below about 5 K in some samples.

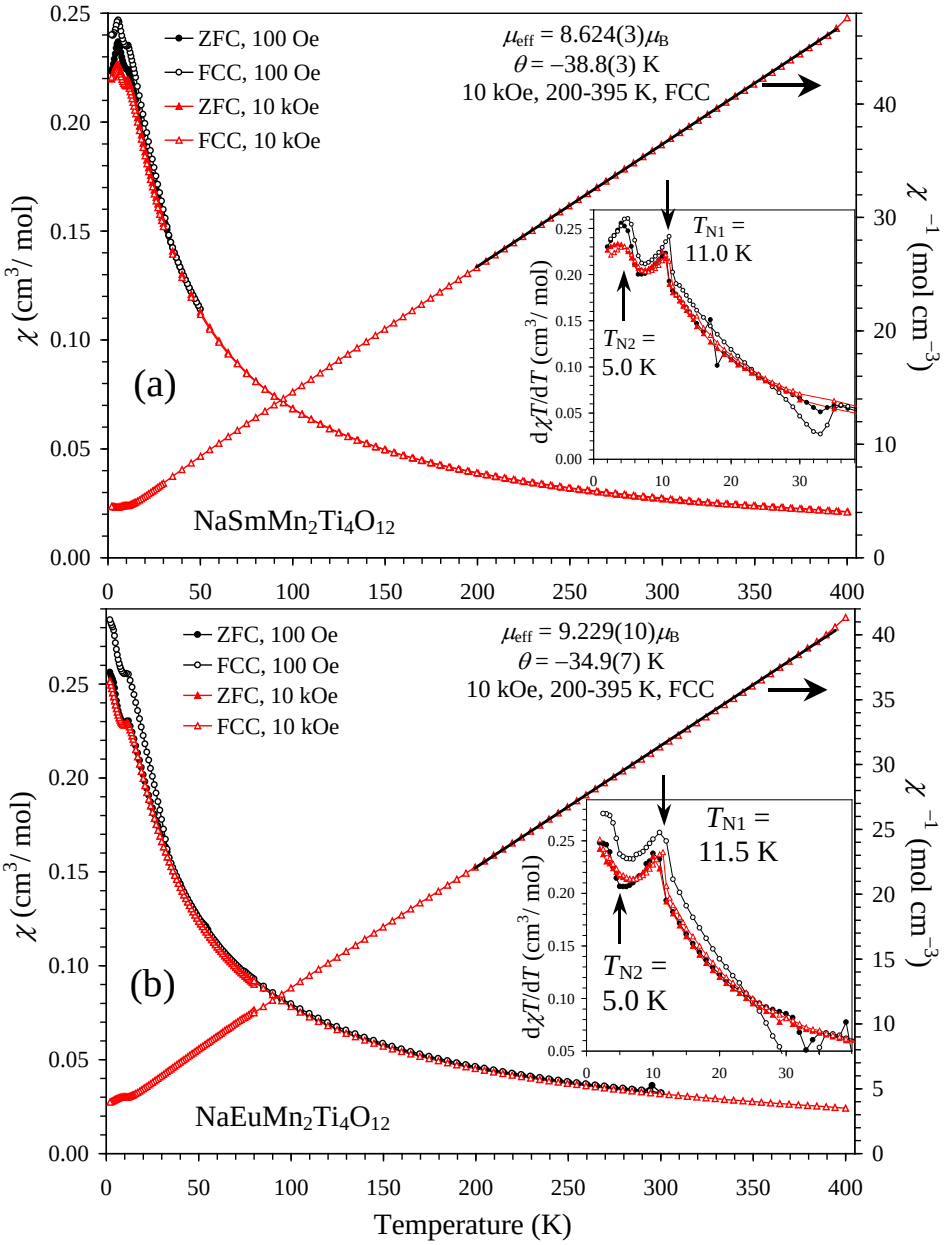

Figure 5. ZFC (filled symbols) and FCC (empty symbols) dc magnetic susceptibility ($\chi = M/H$) curves of (a) $NaSmMn_2Ti_4O_{12}$ and (b) $NaEuMn_2Ti_4O_{12}$ measured at 100 Oe and 10 kOe (left-hand axes). Right-hand axes give the FCC χ^{-1} versus T curves at 10 kOe with the Curie-Weiss fit and fitting parameters. Insets show the d(χT)/dT versus T curves below 40 K to emphasize magnetic anomalies.

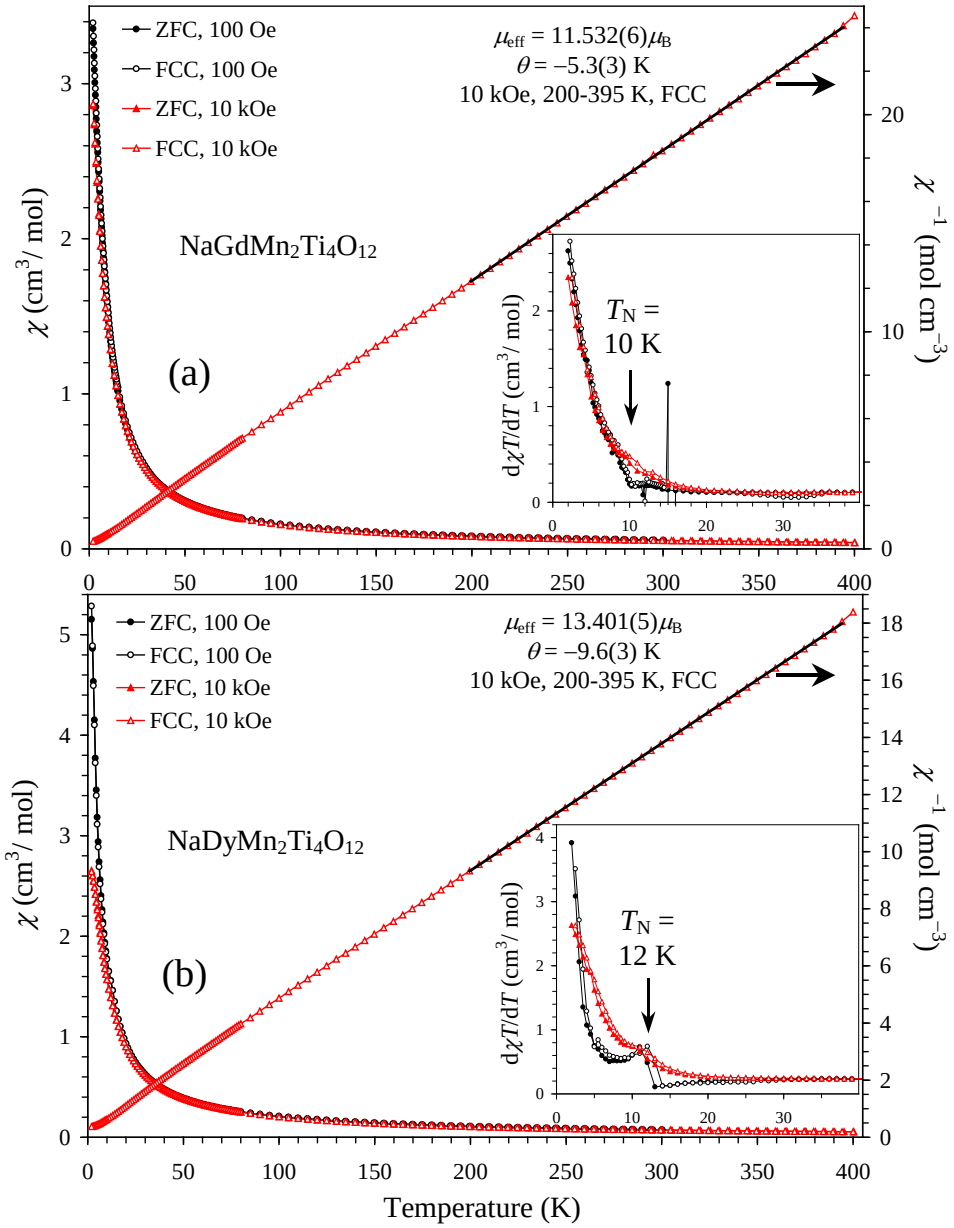

Figure 6. ZFC (filled symbols) and FCC (empty symbols) dc magnetic susceptibility ($\chi = M/H$) curves of (a) $NaGdMn_2Ti_4O_{12}$ and (b) $NaDyMn_2Ti_4O_{12}$ measured at 100 Oe and 10 kOe (left-hand axes). Right-hand axes give the FCC χ^{-1} versus T curves at 10 kOe with the Curie-Weiss fit and fitting parameters. Insets show the d(χT)/dT versus T curves below 40 K to emphasize magnetic anomalies.

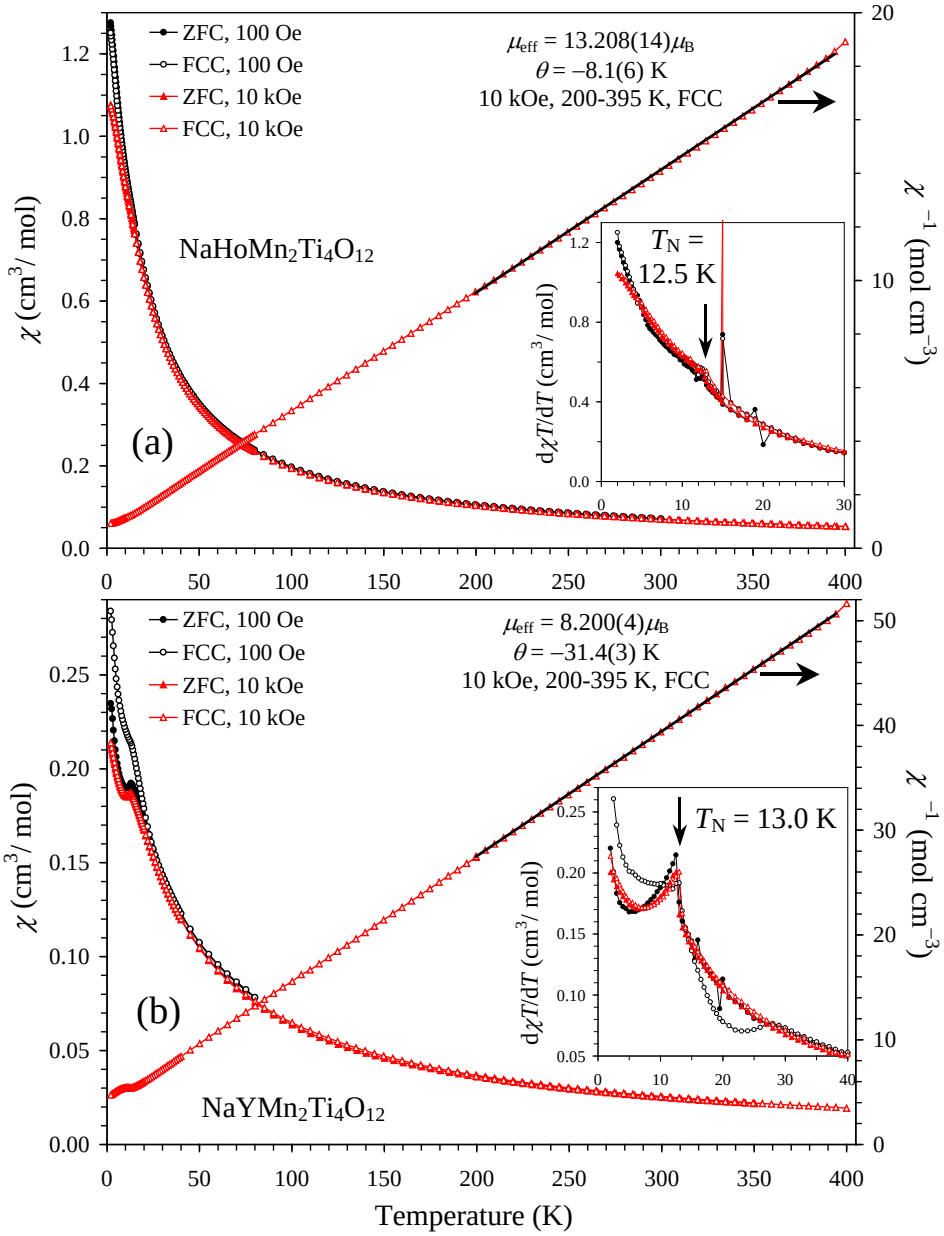

Figure 7. ZFC (filled symbols) and FCC (empty symbols) dc magnetic susceptibility ($\chi = M/H$) curves of (a) $NaHoMn_2Ti_4O_{12}$ and (b) $NaYMn_2Ti_4O_{12}$ measured at 100 Oe and 10 kOe (left-hand axes). Right-hand axes give the FCC χ^{-1} versus T curves at 10 kOe with the Curie-Weiss fit and fitting parameters. Insets show the d(χT)/dT versus T curves below 40 K to emphasize magnetic anomalies.

The fitting results with eq. (1) are summarized in Table 4. The Curie-Weiss linear behavior of the inverse susceptibilities was observed from 400 K down to almost T_N. The experimental effective magnetic moments were close to the calculated ones in all the samples, and the negative Weiss temperatures confirm the dominated antiferromagnetic interactions.

Table 4. **Temperatures of Magnetic Anomalies and Parameters of the Curie-Weiss Fits and *M* versus *H* curves at *T* = 5 K for $NaRMn_2Ti_4O_{12}$**

R	T_N (K)	μ_{eff} (μ_B/f.u.)	μ_{calc} (μ_B/f.u.)	θ (K)	M_S (μ_B/f.u.)
Sm	10.5, 5.0	8.624(3)	8.500	–38.8(3)	2.796
Eu	11.5, 5.0	9.229(10)	9.031	–34.9(7)	2.959
Gd	10.0	11.532(6)	11.576	–5.3(3)	10.559
Dy	12.0	13.401(5)	13.504	–9.6(3)	7.917
Ho	12.5	13.208(14)	13.348	–8.1(6)	7.355
Y	13.0	8.200(4)	8.367	–31.4(3)	2.497

The Curie-Weiss fits are performed between 200 and 395 K using the FCC χ^{-1} versus T data at 10 kOe.
M_S is the magnetization value at T = 5 K and H = 70 kOe; the remnant magnetization (M_R) is nearly zero at T = 5 K, and the coercive field (H_C) is nearly zero T = 5 K. μ_{calc} is calculated using 1.5μ_B for Sm^{3+}, 3.4μ_B for Eu^{3+}, 8.0μ_B for Gd^{3+}, 10.6μ_B for Dy^{3+}, 10.4μ_B for Ho^{3+}, and 5.916μ_B for Mn^{2+}.
T_N values were determined from peaks on the 100 Oe FCC $d(\chi T)/dT$ versus T curves.

Some samples showed a weak divergence between the 100 Oe ZFC and FCC curves and small anomalies on the 100 Oe d(χT)/dT versus T curves near 33 K (R = Sm and Eu), 36 K (R = Gd), and 28 K (R = Y). These temperatures are close to T_N of $MnCO_3$ (T_N = 34-35 K), and these additional magnetic anomalies could originate from this impurity, which shows canted antiferromagnetic properties,[37] even in an amount below the detection limit of synchrotron XRPD. Any contributions from the impurity disappear in high magnetic fields (10 kOe).

M versus *H* curves at T = 5 K were nearly linear without any hysteresis for $NaRMn_2Ti_4O_{12}$ with R = Sm, Eu, and Y (Figure 8a) suggesting pure antiferromagnetic behavior. An S-type shape was observed for $NaRMn_2Ti_4O_{12}$ with R = Gd, Dy, and Ho

(Figure 8b) from the strong paramagnetic contributions of rare-earth cations, but no hysteresis was observed at T = 5 K. A tiny hysteresis opened at T = 1.8-2 K (Figures 8, S12, and S13) in samples that show a strong additional low-temperature specific heat anomaly (R = Sm and Dy).

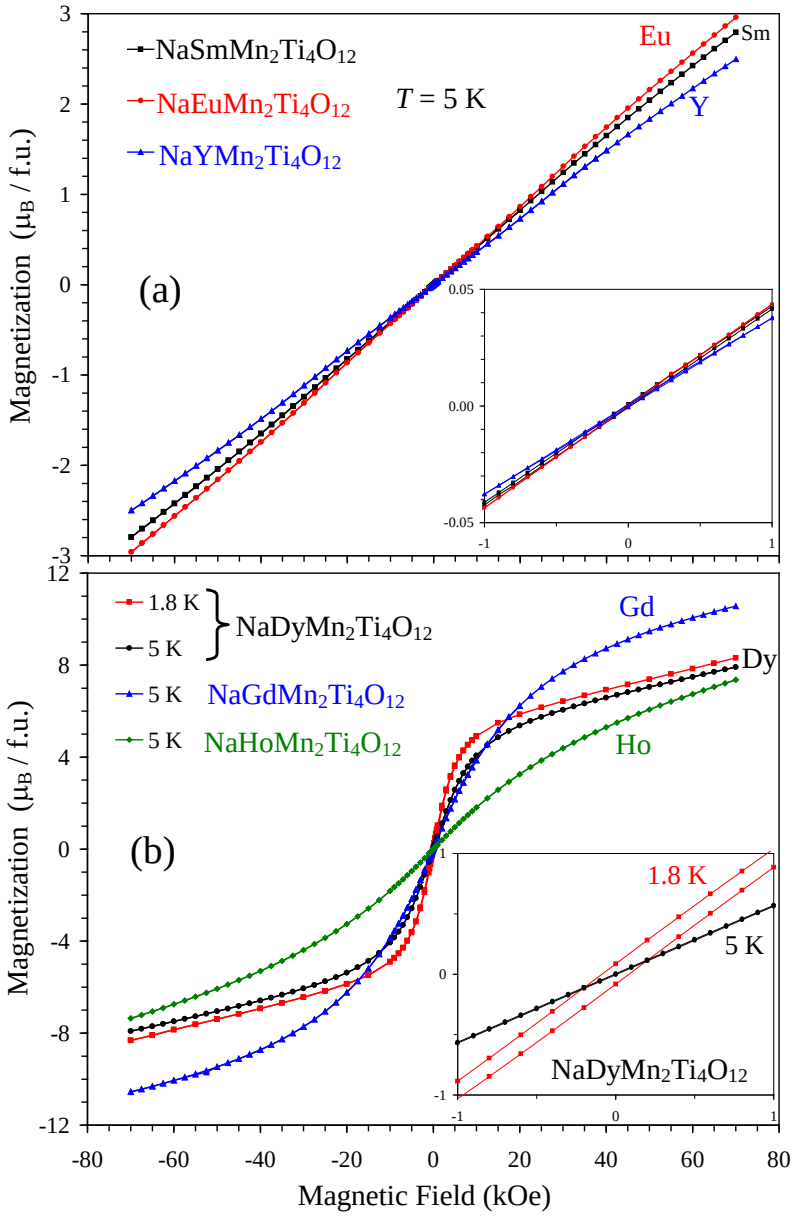

Figure 8. M versus H curves of $NaRMn_2Ti_4O_{12}$ (a) for R = Sm, Eu, and Y at T = 5 K and (b) for R = Dy at T = 1.8 and 5 K and for R = Gd and Ho at T = 5 K. Insets show details near the origin. Additional details near the origin are given on Figure S12.

Specific heat measurements confirmed long-range magnetic orders at T_N in all the samples (Figures 9 and 10). But all the samples showed additional magnetic anomalies at lower temperature. Specific heat data (plotted as C_P/T versus T) of $NaRMn_2Ti_4O_{12}$ with R = Eu, Ho, and Y were qualitatively similar to each other (see also Figures S14 and S15): (1) in addition to a sharp peak at T_N there was a hump near 8 K at H = 0 Oe and (2) a magnetic field of 90 kOe just slightly decreased T_N by about 1.5 K keeping the hump. The C_P/T versus T values of $NaGdMn_2Ti_4O_{12}$ sharply increased down to 2 K at H = 0 Oe, and a magnetic field of 90 kOe suppressed this increase; the similar bahavior of C_P/T versus T curves was observed in $GdMn_7O_{12}$.[38] C_P/T versus T curves of $NaRMn_2Ti_4O_{12}$ with R = Sm and Dy showed a strong additional broad anomaly centered at 3.5 K and 2.8 K, respectively, at H = 0 Oe. C_P/T versus T curves of $NaDyMn_2Ti_4O_{12}$ at H = 90 kOe were qualitatively similar with those of R = Eu, Ho, and Y, that is, the broad anomaly near 2.8 K was suppressed. A magnetic field of 90 kOe had small effects in case of $NaSmMn_2Ti_4O_{12}$.

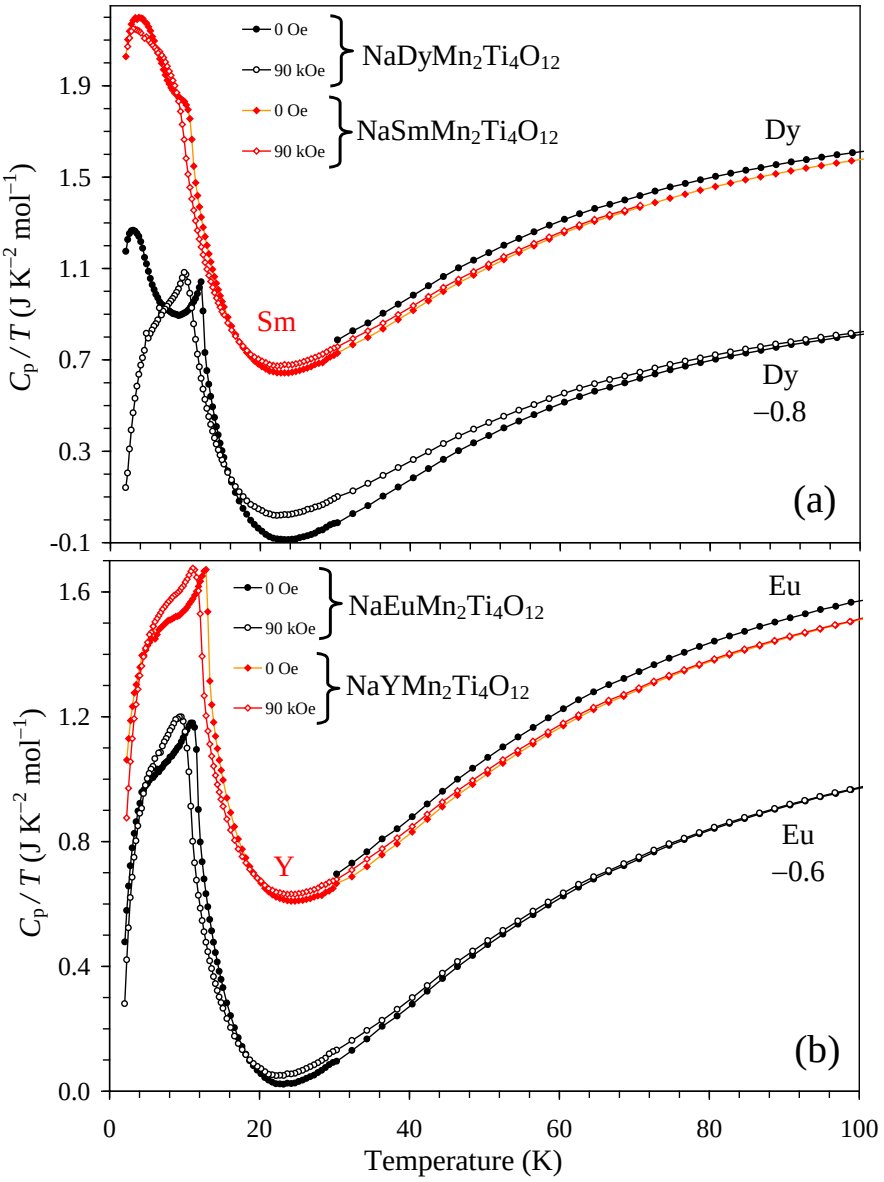

Figure 9. Specific heat data of $NaRMn_2Ti_4O_{12}$ plotted as C_p/T versus T with (a) R = Sm and Dy and (b) R = Eu and Y. Measurements were performed on cooling at H = 0 Oe (filled symbols) and 90 kOe (empty symbols). For R = Dy and Eu, the original data at H = 0 Oe between 30 and 100 K and shifted (for the clarity) data are shown; the shift values are given on the figure.

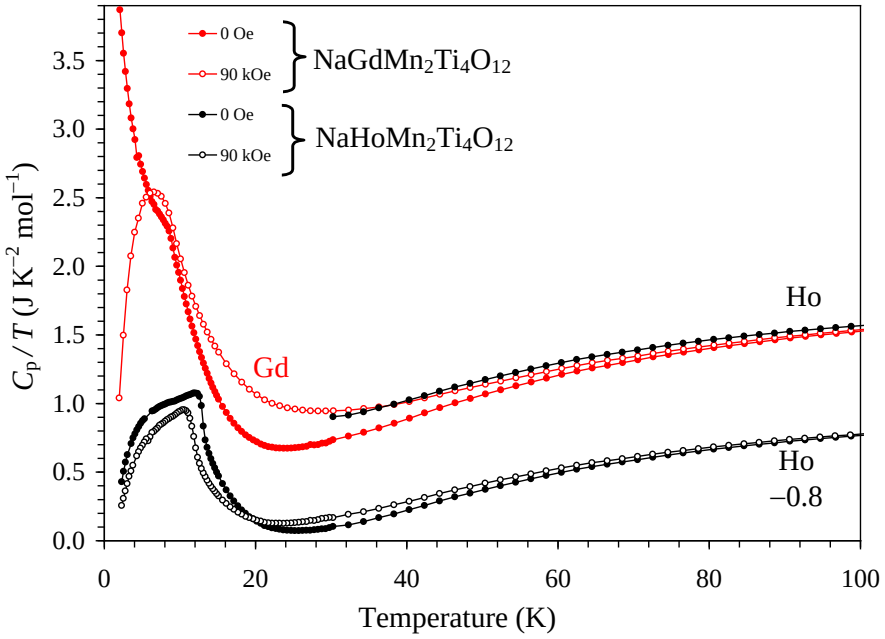

Figure 10. Specific heat data of $NaRMn_2Ti_4O_{12}$ plotted as C_p/T versus T with R = Gd and Ho. Measurements were performed on cooling at H = 0 Oe (filled symbols) and 90 kOe (empty symbols). For R = Ho, the original data at H = 0 Oe between 30 and 100 K and shifted (for the clarity) data are shown; the shift value is given on the figure.

The *mm*2 R site symmetry implies that the crystal electric field ground state of R ions with half-integer total angular momentum, *J*, (e.g. Sm, Gd, and Dy) will be composed of a single Kramers doublet. If the degeneracy of the Kramers doublet is lifted by long-range magnetic ordering, a low temperature Schottky anomaly might be expected to occur in the specific heat, as observed. In an applied high magnetic field the low temperature Schottky anomaly will be suppressed, and powder averaging will instead result in the respective magnetic entropy being 'spread out' over a wide temperature range.

3.5. Neutron Diffraction Studies of $NaDyMn_2Ti_4O_{12}$. The R = Dy sample was selected for neutron diffraction studies for the following reasons: (1) it does not have a *Pnma* impurity, (2) it shows two possible magnetic transitions, and (3) among the R = Sm, Eu, Gd, and Dy samples without a *Pnma* impurity, the R = Dy sample has the smallest neutron absorption coefficient. Measurements were performed at 20 K in the paramagnetic state just above T_{N1}, at 6 K between T_{N2} and T_{N1}, and at 1.5 K below T_{N2}, to gain insight into long-range magnetic ordering and the possible origin of the second magnetic

transition, which was not observed in $CaMnTi_2O_6$[19,20]. Additional information and general support for the structural model obtained from synchrotron X-ray diffraction was also established by structural refinement in the paramagnetic phase. The elastic neutron powder diffraction pattern measured at 20 K was used to refine the crystal structure model of the paramagnetic phase of $NaDyMn_2Ti_4O_{12}$. The initial XRPD model was in good agreement with the data; however, a significant improvement of the fitting was obtained by introducing about 6 % Dy/Mn occupational disorder between A and (A′, A″) sites (R_{wp} = 4.18 %, R_P = 4.49 %, and R_F = 4.70 % were improved to R_{wp} = 3.74 %, R_P = 4.20 %, and R_F = 4.14 %). Such site disorder has been observed in other A-site columnar-ordered perovskites.[33] We note that an equivalent quality of the fitting could be achieved by introducing occupational disorder between Na and Mn, however, the amount of Na in the A′ and A″ sites was found to be larger (12.0 %) in this case. The two scenarios with Dy/Mn or Na/Mn anti-site substitutions were considered separately, as parameter correlations prevent the simultaneous refinement of occupancies for all three cations. Neutron diffraction gave further evidence for splitting of the Mn1 site as the thermal parameter obtained for Mn when constrained to the ideal Mn1 site was unphysically large (B ~7 Å^2), and also found to be independent of the anti-site cation disorder. A TiO_2 impurity phase was also present in small amount 3.3(2) mass % in the measured sample. Experimental, calculated, and difference neutron diffraction patterns of $NaDyMn_2Ti_4O_{12}$ at 20 K are plotted on Figure 2b. Structural parameters of $NaDyMn_2Ti_4O_{12}$ at 20 K and 6 K are summarized in Tables S7 and S8.

Below the magnetic phase transition temperature new diffraction peaks were observed in the diffraction pattern. These peaks could be fit using the same profile parameters as used for the paramagnetic refinement, indicating that the magnetic order is well correlated in all three dimensions. The three strongest magnetic diffraction peaks (see Figure 11 inset) could be indexed {102}, {212}, and {100} with respect to the paramagnetic crystal structure. Symmetry analysis using ISODISTORT[39] gave four irreducible representations for the Mn lattice in which Mn1 was considered sitting in its ideal non-split position. We consider four symmetry adapted modes, F_i, A_i, C_i, and G_i, as defined in Table S9, where the subscript i denotes the direction of the magnetic moments. Broadly speaking, these modes describe magnetic structures with either ferromagnetic (FM) or antiferromagnetic

(AFM) nearest-neighbour interactions and moments parallel or perpendicular to the tetragonal *c*-axis. Table S10 classifies combinations of these modes in terms of the irreducible representations. Table S9 also lists the diffraction reflection conditions for the four symmetry adapted modes. The measured magnetic intensities are at *hkl* positions that satisfy the diffraction condition $l = 2n$ and $h+k = 2n+1$, where n is an integer. These diffraction conditions uniquely determine a *C*-type magnetic structure of the Mn lattice, according to which AFM coupled layers in the *ab*-plane are FM coupled along the *c*-crystallographic direction. Furthermore, the observation of the magnetic diffraction peak {100}, together with the absence of the (001) peak, uniquely determines the moment direction to be parallel to the tetragonal *c*-axis (i.e. Γ_2^- with $P4_2'/n'm'c$, #137.512 magnetic space group). This magnetic structure was refined against the data, an excellent agreement factor R_{mag} = 3.34 % was achieved, and a Mn magnetic moment of 2.58(2)μ_B at 6 K was found, which is noticeably reduced compared with the expected moment of 5μ_B for Mn^{2+}. The same magnetic structure and similar magnetic moment of 2.58μ_B were found in $Ca_{1.4}Mn_{0.6}Ti_2O_6$ in the ground state at 1.5 K.[20] We note that the symmetry of the system (Γ_2^-) allows the moments at the A′ and A″ sites to be refined independently, however, this admixes an A_z mode that would produce magnetic peaks in position of the diffractogram where nothing was detected. Surprisingly, the magnetic Bragg peaks broaden at 1.5 K below the second magnetic transition, revealing a transition to a state with short-range magnetic correlations (Figure 11a inset). The origin of this transition is not clear and will be the subject of future studies, but it could be related to the polarization of Dy magnetic moments together with some Na/Dy occupational disorder in the A sites.

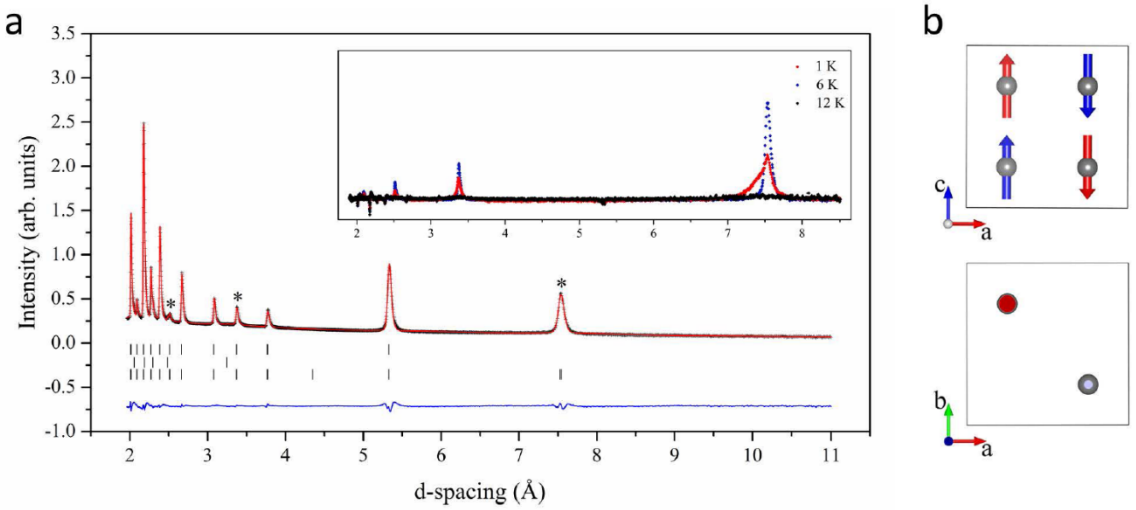

Figure 11. (a) Neutron powder diffraction pattern at T = 6 K for $NaDyMn_2Ti_4O_{12}$. Data and fit are shown as black crosses and a red line, respectively, and their difference is drawn as a blue line at the bottom of the panel (reliability factors: R_p = 3.41 %, R_{wp} = 3.03 %, R_{Bragg} = 3.56 % (nuclear) and R_{Bragg} = 3.34 % (magnetic)). The tick marks show possible Bragg reflection positions for the main perovskite phase (first row); TiO_2 impurity (second row); and *C*-type magnetic structure of the manganese A′ and A″ lattice of the main perovskite phase (third row). Peaks with magnetic intensity contributions are marked by an asterisk and their temperature evolutions is shown in the inset. (b) View of the *C*-type magnetic structure along different crystallographic directions. Mn atoms in the square planar and in the tetrahedral coordination sites are shown with blue and red arrows, respectively.

3.6. Dielectric Properties of $NaRMn_2Ti_4O_{12}$. Dielectric measurements showed the existence of two plateaus: a low-temperature plateau with dielectric constant of about 100 and a high-temperature plateau with dielectric constant of about 600. The dielectric constant changed in a step-like manner between the two plateaus, and the temperature of the step-like change strongly depends on frequency. At the same time, very strong dielectric loss peaks appear at the temperature of the step-like dielectric change. The low-temperature plateau was quite narrow in the case of $NaGdMn_2Ti_4O_{12}$ (Figure 12), while it was wider in case of $NaDyMn_2Ti_4O_{12}$ (Figure 13) and $NaEuMn_2Ti_4O_{12}$ (Figures S16 and S17). The temperature dependence of dielectric constant of $NaRMn_2Ti_4O_{12}$ resembles that

of $CaCu_3Ti_4O_{12}$ except for one difference; the high-temperature plateau does not reach giant values as in $CaCu_3Ti_4O_{12}$.[13-15] Therefore, we can assume that changes in the dielectric constant occur via the same mechanism in $NaRMn_2Ti_4O_{12}$ and $CaCu_3Ti_4O_{12}$, that is, there is an electrical inhomogeneity of $NaRMn_2Ti_4O_{12}$ ceramics with semiconducting grains and insulating grain boundaries (or vice versa). But we emphasize that $NaRMn_2Ti_4O_{12}$ ceramics were highly insulating even at room temperature, and the total resistivity of $NaRMn_2Ti_4O_{12}$ ceramics could not be measured with a PPMS system.

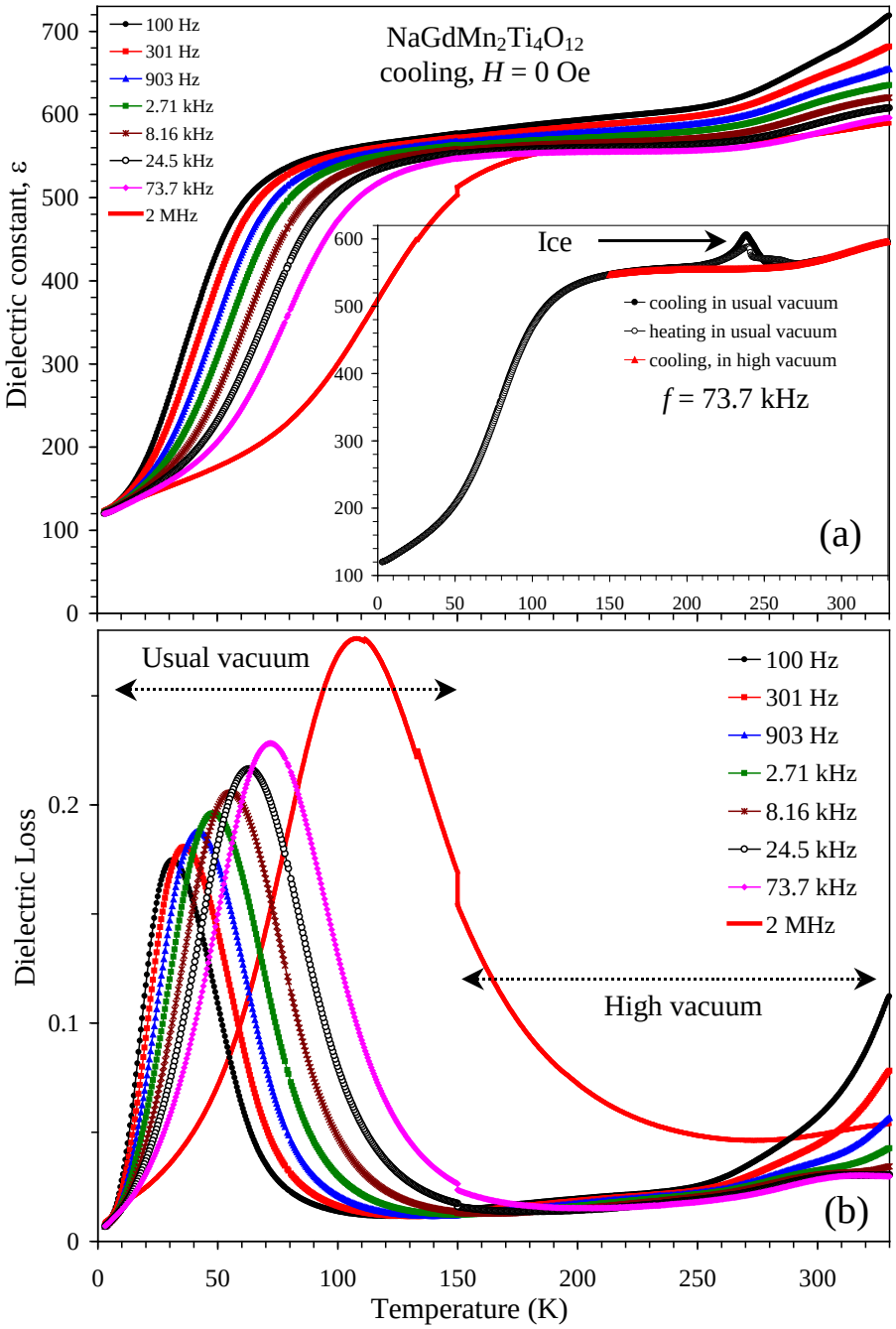

Figure 12. (a) Dielectric constant and (b) dielectric loss of $NaGdMn_2Ti_4O_{12}$ as a function of temperature measured at H = 0 Oe on heating at different frequencies. Measurements in usual and high vacuum conditions were combined at 150 K. The inset gives dielectric constant in usual (3-330 K) and high vacuum (150-330 K) conditions to emphasize extrinsic contributions near 220-270 K in usual vacuum conditions.

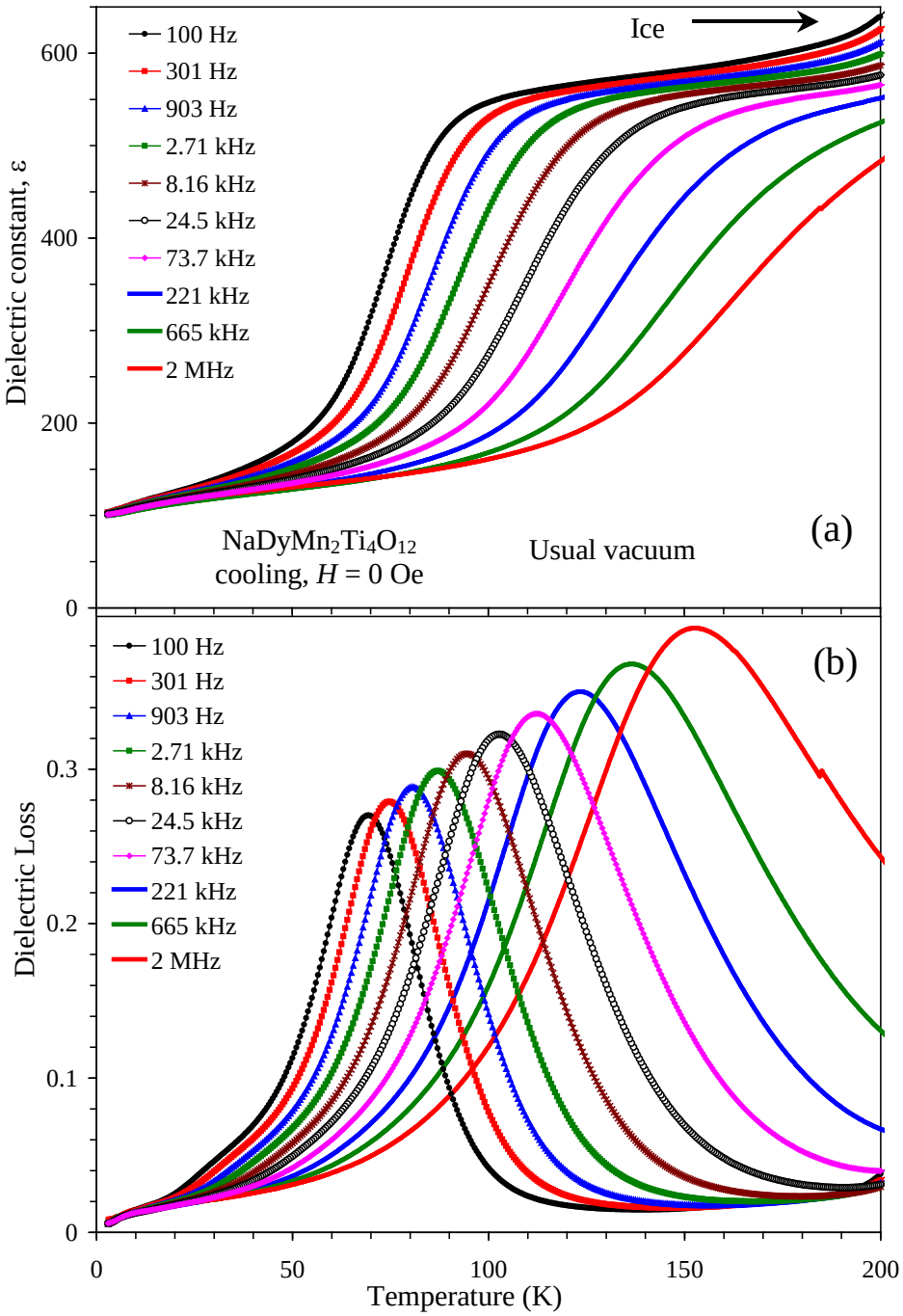

Figure 13. (a) Dielectric constant and (b) dielectric loss of $NaDyMn_2Ti_4O_{12}$ as a function of temperature measured at H = 0 Oe on cooling at different frequencies. Measurements were performed in usual vacuum conditions, the data are shown below 200 K, where extrinsic contributions are absent.

4. Conclusions

A-site columnar-ordered quadruple perovskites $NaRMn_2Ti_4O_{12}$ with R = Sm, Eu, Gd, Dy, Ho, and Y were prepared by a high-pressure high-temperature method. Structural studies between 1.5 and 300 K based on analysis of powder synchrotron X-ray and neutron diffraction data indicated that they maintain the centrosymmetric paraelectric structure at all temperatures, with Mn^{2+} cations highly disordered at the square-planar site. We have shown a C-type magnetic structure for R = Dy at 6 K, similar to that found in the $CaMnTi_2O_6$ compound. Given similarities in the magnetic susceptibility and heat capacity data, we anticipate the same magnetic structure in all A-site columnar-ordered $NaRMn_2Ti_4O_{12}$ compounds, at least below T_{N1} = 8-13 K. However, additional magnetic features were observed at lower temperatures for R = Sm, Eu, and Dy.

Associated Content

Supporting information

Details of fitting results, DSC, dc and ac magnetic susceptibility, specific heat, and dielectric measurements, structural parameters of $NaDyMn_2Ti_4O_{12}$ at 6 and 20 K and other structural tables (PDF).

Author Information

Corresponding Author

Alexei.Belik@nims.go.jp

Notes

The authors declare no competing financial interest.

Acknowledgements

This work was partly supported by JSPS KAKENHI Grant Numbers JP20H05276 and 19H05819, a research grant (40-37) from Nippon Sheet Glass Foundation for Materials Science and Engineering, and Innovative Science and Technology Initiative for Security (Grant Number JPJ004596) from Acquisition, Technology, and Logistics Agency (ATLA), Japan. R.S. acknowledges support from EPSRC Grant No. EP/M020517/1, entitled Oxford Quantum Materials Platform Grant, and R.D.J. acknowledges support from a Royal Society

University Research Fellowship. The synchrotron radiation experiments were performed at SPring-8 with the approval of the NIMS Synchrotron X-ray Station (Proposal Numbers: 2018B4502 and 2019A4501).

References

(1) Dawber, M.; Rabe, K. M.; Scott, J. F. Physics of Thin-Film Ferroelectric Oxides. *Rev. Mod. Phys.* **2005**, *77*, 1083-1130.

(2) Izyumskaya, N.; Alivov, Y.; Morkoç, H. Oxides, Oxides, and More Oxides: High-κ Oxides, Ferroelectrics, Ferromagnetics, and Multiferroics. *Crit. Rev. Solid State Mater. Sci.* **2009**, *34*, 89-179.

(3) Izyumskaya, N.; Alivov, Y. I.; Cho, S. J.; Morkoç, H.; Lee, H.; Kang, Y. S. Processing, Structure, Properties, and Applications of PZT Thin Films. *Crit. Rev. Solid State Mater. Sci.* **2007**, *32*, 111-202.

(4) Kennedy, B. J.; Zhou, Q.; Zhao, S.; Jia, F.; Ren, W.; Knight, K. S. Low-Temperature Structure and the Ferroelectric Phase Transitions in the $CdTiO_3$ Perovskite. *Phys. Rev. B: Condens. Matter Mater. Phys.* **2017**, *96*, 214105.

(5) Müller, K. A.; Burkard, H. $SrTiO_3$: An Intrinsic Quantum Paraelectric Below 4 K. *Phys. Rev. B: Condens. Matter Mater. Phys.* **1979**, *19*, 3593.

(6) Itoh, M.; Wang, R.; Inaguma, Y.; Yamaguchi, T.; Shan, Y. J.; Nakamura, T. Ferroelectricity Induced by Oxygen Isotope Exchange in Strontium Titanate Perovskite. *Phys. Rev. Lett.* **1999**, *82*, 3540-3543.

(7) Jang, H. W.; Kumar, A.; Denev, S.; Biegalski, M. D.; Maksymovych, P.; Bark, C. W.; Nelson, C. T.; Folkman, C. M.; Baek, S. H.; Balke, N.; Brooks, C. M.; Tenne, D. A.; Schlom, D. G.; Chen, L. Q.; Pan, X. Q.; Kalinin, S. V.; Gopalan, V.; Eom, C. B. Ferroelectricity in Strain-Free $SrTiO_3$ Thin Films. *Phys. Rev. Lett.* **2010**, *104*, 197601.

(8) Taniguchi, H.; Shan, Y. J.; Mori, H.; Itoh, M. Critical Soft-Mode Dynamics and Unusual Anticrossing in $CdTiO_3$ Studied by Raman Scattering. *Phys. Rev. B: Condens. Matter Mater. Phys.* **2007**, *76*, 212103.

(9) Inaguma, Y.; Sohn, J.-H.; Kim, I.-S.; Itoh, M.; Nakamura, T. Quantum Paraelectricity in a Perovskite $La_{1/2}Na_{1/2}TiO_3$. *J. Phys. Soc. Jpn.* **1992**, *61*, 3831-3832.

(10) Shan, Y. J.; Nakamura, T.; Inaguma, Y.; Itoh, M. Preparation and Dielectric Characterizations of the Novel Perovskite-type Oxides $(Ln_{1/2}Na_{1/2})TiO_3$ (Ln=Dy, Ho, Er, Tm, Yb, Lu). *Solid State Ionics* **1998**, *108*, 123-128.

(11) Gorfman, S.; Glazer, A. M.; Noguchi, Y.; Miyayama, M.; Luo, H.; Thomas, P. A. Observation of a Low-symmetry Phase in $Na_{0.5}Bi_{0.5}TiO_3$ Crystals by Optical Birefringence Microscopy. *J. Appl. Crystallogr.* **2012**, *45*, 444-452.

(12) McQuade, R. R.; Dolgos, M. R. A Review of the Structure-property Relationships in Lead-free Piezoelectric $(1-x)Na_{0.5}Bi_{0.5}TiO_3–(x)BaTiO_3$. *J. Solid State Chem.* **2016**, *242*, 140-147.

(13) Subramanian, M. A.; Li, D.; Duan, N.; Reisner, B. A.; Sleight, A. W. High Dielectric Constant in $ACu_3Ti_4O_{12}$ and $ACu_3Ti_3FeO_{12}$ Phases. *J. Solid State Chem.* **2000**, *151*, 323-325.

(14) Homes, C. C.; Vogt, T.; Shapiro, S. M.; Wakimoto, S.; Ramirez, A. P. Optical Response of High-Dielectric-Constant Perovskite-Related Oxide. *Science* **2001**, *293*, 673-676.

(15) Liu, L.; Ren, S.; Liu, J.; Han, F.; Zhang, J.; Peng, B.; Wang, D.; Bokov, A. A.; Ye, Z. G. Localized Polarons and Conductive Charge Carriers: Understanding $CaCu_3Ti_4O_{12}$ over a Boad Temperature Range. *Phys. Rev. B: Condens. Matter Mater. Phys.* **2019**, *99*, 094110.

(16) Adams, T. B.; Sinclair, D. C.; West, A. R. Giant Barrier Layer Capacitance Effects in $CaCu_3Ti_4O_{12}$ Ceramics. *Adv. Mater.* **2002**, *14*, 1321-1323.

(17) Ferrarelli, M. C.; Adams, T. B.; Feteira, A.; Sinclair, D. C.; West, A. R. High Intrinsic Permittivity in $Na_{1/2}Bi_{1/2}Cu_3Ti_4O_{12}$. *Appl. Phys. Lett.* **2006**, *89*, 212904.

(18) Ferrarelli, M. C.; Sinclair, D. C.; West, A. R. Possible Incipient Ferroelectricity in Mn-doped $Na_{1/2}Bi_{1/2}Cu_3Ti_4O_{12}$. *Appl. Phys. Lett.* **2009**, *94*, 212901.

(19) Aimi, A.; Mori, D.; Hiraki, K.; Takahashi, T.; Shan, Y. J.; Shirako, Y.; Zhou, J. S.; Inaguma, Y. High-Pressure Synthesis of A-Site Ordered Double Perovskite $CaMnTi_2O_6$ and Ferroelectricity Driven by Coupling of A-Site Ordering and the Second-Order Jahn–Teller Effect. *Chem. Mater.* **2014**, *26*, 2601–2608.

(20) Li, Z.; Cho, Y.; Li, X.; Li, X.; Aimi, A.; Inaguma, Y.; Alonso, J. A.; Fernandez-Diaz, M. T.; Yan, J.; Downer, M. C.; Henkelman, G.; Goodenough, J. B.; Zhou, J. New Mechanism for Ferroelectricity in the Perovskite $Ca_{2-x}Mn_xTi_2O_6$ Synthesized by Spark Plasma Sintering. *J. Am. Chem. Soc.* **2018**, *140*, 2214−2220.

(21) Belik, A. A. Rise of A-site Columnar-Ordered $A_2A'A''B_4O_{12}$ Quadruple Perovskites with Intrinsic Triple Order. *Dalton Trans.* **2018**, *47*, 3209–3217.

(22) Tanaka, M.; Katsuya, Y.; Yamamoto, A. A New Large Radius Imaging Plate Camera for High-resolution and High-throughput Synchrotron X-ray Powder Diffraction by Multiexposure Method, *Rev. Sci. Instrum*. **2008**, *79*, 075106.

(23) Tanaka, M.; Katsuya, Y.; Matsushita, Y.; Sakata, O. Development of a Synchrotron Powder Diffractometer with a One-dimensional X-ray Detector for Analysis of Advanced Materials, *J. Ceram. Soc. Jpn*. **2013**, *121*, 287–290.

(24) Izumi, F.; Ikeda, T. A Rietveld-analysis Program RIETAN-98 and its Applications to Zeolites, *Mater. Sci. Forum*, **2000**, *321-324*, 198–205.

(25) Chapon, L. C.; Manuel, P.; Radaelli, P. G.; Benson, C.; Perrott, L.; Ansell, S.; Rhodes, N. J.; Raspino, D.; Duxbury, D.; Spill, E.; Norris, J. Wish: the New Powder and Single Crystal Magnetic Diffractometer on the Second Target Station. *Neutron News* **2011**, *22*, 22–25.

(26) Rodriguez, C. J. Recent Advances in Magnetic Structure Determination by Neutron Powder Diffraction. *Phys. B* **1993**, *193*, 55–69.

(27) Kurtz, S. K.; Perry, T. T. A Powder Technique for the Evaluation of Nonlinear Optical Materials, *J. Appl. Phys.* **1968**, *39*, 3798-3813.

(28) Inaguma, Y.; Aimi, A.; Shirako, Y.; Sakurai, D.; Mori, D.; Kojitani, H.; Akaogi, M.; Nakayama, M. High-Pressure Synthesis, Crystal Structure, and Phase Stability Relations of a $LiNbO_3$-Type Polar Titanate $ZnTiO_3$ and Its Reinforced Polarity by the Second-Order Jahn–Teller Effect, *J. Am. Chem. Soc.* **2014**, *136*, 2748–2756.

(29) Leinenweber, K.; Parise, J. High-pressure Synthesis and Crystal Structure of $CaFeTi_2O_6$, a New Perovskite Structure Type, *J. Solid State Chem*. **1995**, *114*, 277–281.

(30) Solana-Madruga, E.; Arevalo-Lopez, A. M.; Dos Santos-Garcia, A. J.; Urones-Garrote, E.; Avila-Brande, D.; Saez-Puche, R.; Attfield, J. P. Double Double Cation Order in the High-Pressure Perovskites $MnRMnSbO_6$. *Angew. Chem. Int. Ed.* **2016**, *55*, 9340–9344.

(31) Zhang, L.; Matsushita, Y.; Yamaura, K.; Belik, A. A. Five-fold Ordering in High-pressure Provskites RMn_3O_6 (R = Gd-Tm and Y). *Inorg. Chem.* **2017**, *56*, 5210–5218.

(32) Belik, A. A.; Khalyavin, D. D.; Zhang, L.; Matsushita, Y.; Katsuya, Y.; Tanaka, M.; Johnson, R. D.; Yamaura, K. Intrinsic Triple Order in A-site Columnar-ordered Quadruple Perovskites: Proof of Concept. *ChemPhysChem*. **2018**, *19*, 2449–2452.

(33) Belik, A. A.; Zhang, L.; Liu, R.; Khalyavin, D. D.; Katsuya, Y.; Tanaka, M.; Yamaura, K. Valence Variations by B-Site Doping in A-Site Columnar-Ordered Quadruple Perovskites $Sm_2MnMn(Mn_{4-x}Ti_x)O_{12}$ with $1 \le x \le 3$. *Inorg. Chem.* **2019**, *58*, 3492–3501.

(34) Shannon, R. D. Revised Effective Ionic Radii and Systematic Studies of Interatomic Distances in Halides and Chalcogenides. *Acta Crystallogr., Sect. A: Cryst. Phys., Diffr., Theor. Gen. Crystallogr.* **1976**, *32*, 751–767.

(35) Brese, N. E.; O'Keeffe, M. Bond-valence Parameters for Solids, *Acta Crystallogr., Sect. B: Struct. Sci*. **1991**, *47*, 192–197.

(36) Belik, A. A.; Matsushita, Y.; Kumagai, Y.; Katsuya, Y.; Tanaka, M.; Stefanovich, S. Yu.; Lazoryak, B. I.; Oba F.; Yamaura, K. Complex Structural Behavior of $BiMn_7O_{12}$ Quadruple Perovskite. *Inorg. Chem.* **2017**, *56*, 12272–12281.

(37) Maartense, I. Magnetic Properties of Fe^{2+}-doped $MnCO_3$. *Phys. Rev. B: Condens. Matter Mater. Phys.* **1972**, *6*, 4324–4331.

(38) Zhang, L.; Terada, N.; Johnson, R. D.; Khalyavin, D. D.; Manuel, P.; Katsuya, Y.; Tanaka, M.; Matsushita, Y.; Yamaura, K.; Belik, A. A. High-Pressure Synthesis, Structures, and Properties of Trivalent A-Site-Ordered Quadruple Perovskites RMn_7O_{12} (R = Sm, Eu, Gd, and Tb). *Inorg. Chem.* **2018**, *57*, 5987–5998.

(39) Stokes, H. T.; Van Orden, S.; Campbell, B. J. ISOSUBGROUP: An Internet Tool for Generating Isotropy Subgroups of Crystallographic Space Groups. *J. Appl. Crystallogr.* **2016**, *49*, 1849–1853.

For Table of Contents Only

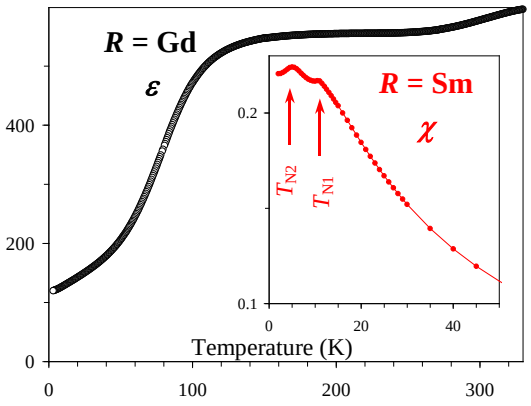

A-site columnar-ordered quadruple perovskites $NaRMn_2Ti_4O_{12}$ with R = Sm, Eu, Gd, Dy, Ho, and Y were prepared by a high-pressure high-temperature method. Their structural, magnetic, and dielectric properties are reported.